11 Topological Semimetals

Andreas P. Schnyder
Max-Planck-Institut für Festkörperforschung
Stuttgart

Contents

E. Pavarini and E. Koch (eds.)
Topology, Entanglement, and Strong Correlations
Modeling and Simulation Vol. 10
Forschungszentrum Jülich, 2020, ISBN 978-3-95806-466-9
http://www.cond-mat.de/events/correl20

1 Introduction

The last decade has witnessed tremendous progress in our understanding of topological band theory. Soon after the discovery of topological insulators [1], it has been realized that topology plays also a significant role in gapless systems, i.e., in topological semimetals [2–7]. Topological semimetals exhibit protected band crossings near the Fermi energy with nonzero topological charges. While the existence of these band crossings has been recognized early on during the development of band theory [8], their fundamental importance has been understood only recently. In the course of the last few years it has been shown that topological band crossing give rise to a variety of interesting phenomena, such as, intrinsic anomalous Hall effects [6], exotic surface states [5], large thermopower, and unusual responses related to quantum anomalies [9]. Because of these properties, topological semimetals could potentially be used for new device applications [10]. E.g., the helical nature of the surface states can be used for low-dissipation transport [11]. The spin-momentum locking of the surface states can be utilized for low-consumption spintronic devices and magnetic memory devices [12]. The high photosensitivity of topological semimetals is of importance for the construction of ultrafast photodetectors [13]. Moreover, many topological semimetals have large thermoelectric responses, which could be of use for high-efficiency energy converters or thermal detectors [14].

There are two different types of topological band crossings, namely, accidental band crossings and symmetry-enforced band crossings. Accidental band crossings are protected by *symmorphic* crystal symmetries and are only perturbatively stable [2]. That is, they can be adiabatically removed by large symmetry-preserving deformations of the Hamiltonian, for example, through pair annihilation. Dirac points and Dirac lines are examples of accidental band crossings, which are protected by parity-time inversion, reflection, or rotation symmetry [7, 15]. Another example is Weyl points, which can be stable even in the absence of symmetries [5, 6]. Accidental band crossings also occur in the Bogoliubov bands of superconductors [2]. Symmetry-enforced band crossings [16–22], however, arise in the presence of *nonsymmorphic* symmetries and are globally stable, i.e., they cannot be removed even by large deformations of the Hamiltonian. That is, these band crossings are required to exist due to nonsymmorphic symmetries alone, independent of material details, such as chemical composition or energetics of the bands.

In these lectures we will discuss both types of band crossings, first focusing on accidental band crossings in Sec. 2 and then studying symmetry-enforced band crossings in Sec. 3. A particular focus will be on nodal-line semimetals, where the band crossings occur along one-dimensional lines in the BZ, close to or at the Fermi energy. But we will also discuss Weyl semimetals, where the band crossings occur at isolated points in the Brillouin zone (BZ).

In the following we will focus on weakly interacting semimetals, which can be described within the single-particle picture. Using the band theory of solids [23], the electronic wavefunctions ψ in a crystal of a semimetal can be classified by their crystal momentum $\mathbf{k}$, which is defined in the periodic BZ. Bloch's theorem tells us that ψ can be expressed in terms of Bloch states $|u_m(\mathbf{k})\rangle$, which are defined in a single unit cell of the crystal. These Bloch states are eigenstates

of the Bloch Hamiltonian $H(\mathbf{k})$,[1]

$$H(\mathbf{k})\,|u_m(\mathbf{k})\rangle = E_m(\mathbf{k})\,|u_m(\mathbf{k})\rangle\,, \tag{1}$$

where m represents the band index. The eigenvalues $E_m(\mathbf{k})$ in the above equation are called Bloch bands and the set $\{E_m(\mathbf{k})\}$ is referred to as the band structure of the solid.
In this lecture we are interested in the crossings between two different bands, $E_m(\mathbf{k})$ and $E_{m'}(\mathbf{k})$, say. That is, we want to know under which conditions the two energies $E_m(\mathbf{k})$ and $E_{m'}(\mathbf{k})$ become degenerate at certain points or lines in the BZ. The main focus will be on electronic band structures of solids. However, the band crossings discussed here can also occur in different contexts, for example, for photonic bands of dielectric superlattices [24], for phonon bands in crystals, for magnon bands in ordered antiferromagnets [25], or for Bogoliubov bands in superconductors [1, 2].
The remainder of these notes are organized as follows. In Sec. 2.1 we will begin by deriving a classification of accidental band crossings protected by time-reversal symmetry, particle-hole symmetry, and/or chiral symmetry. As concrete examples of such accidental band crossings, we will consider, among others, Weyl and nodal-line semimetals (Secs. 2.2 and 2.3). For these examples we will discuss the bulk-boundary correspondence, which relates the nontrivial topology of the band crossing in the bulk to the appearance of surface states. We will also review the quantum anomalies that arise in the low-energy descriptions of these semimetals. Section 3 is devoted to the study of symmetry-enforced band crossings. We will first explain some general properties of nonsymmorphic symmetries and show how these can lead to symmetry-enforced band crossings. Subsequently, two examples of nonsymmorphic band crossings will be discussed: Weyl lines protected by glide reflection in Sec. 3.2 and Dirac lines protected by off-center symmetries in Sec. 3.3. For each of these examples, we present some material realizations and discuss implications for experiments.

2 Accidental band crossings

Accidental band crossings occur, for example, when a hole-like and an electron-like parabolic band in a two-dimensional material overlap, forming two band crossings, as shown in Fig. 1. This band crossing is stable if the two bands have a non-trivial topology and/or opposite symmetry. In general these accidental crossings share the following features:

- They are protected by *symmorphic* crystal symmetries and/or nonspatial symmetries. Here, symmorphic symmetry means a symmetry which leaves at least one point of the real-space crystal invariant. Symmorphic symmetries are point-group symmetries of the crystal, such as rotation or reflection. Nonspatial symmetry refers to a symmetry that dose not transform different lattice sites into each other. I.e., a symmetry that acts locally in real space, such as time-reversal or particle-hole symmetry.

[1] For superconductors the Bloch Hamiltonian should be replaced by a Bogoliubov-de Gennes Hamiltonian.

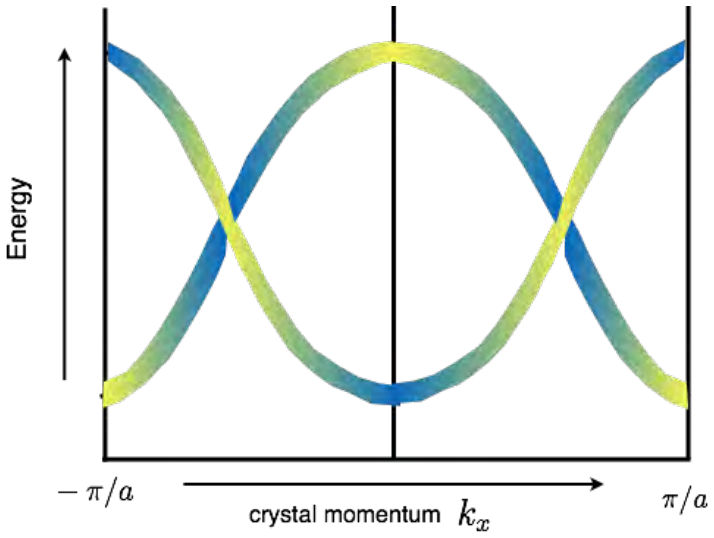

Fig. 1: *When an electron- and hole-like band of different symmetry overlap, they form two accidental band crossings. The color shading indicates some "pseudo-spin" degree of freedom of the Bloch states* $|u_n(\mathbf{k})\rangle$*, which depends on crystal momentum* $\mathbf{k}$*.*

- Accidental band crossings exhibit local topological charges n_{top}. These topological charges are defined in terms of contour integrals, e.g.,

$$n_{\text{top}} = \frac{1}{2\pi} \oint_{\mathcal{C}} \mathcal{F}(\mathbf{k})\, d\mathbf{k} \;\in\; \mathbb{Z}, \tag{2}$$

  where the integration is along the contour $\mathcal{C}$, which encloses the band crossing point or line. Here, $\mathcal{F}(\mathbf{k})$ represents a general curvature function, such as the Berry curvature or the winding number density. These topological charges are quantized to integer values, i.e., $n_{\text{top}} \in \mathbb{Z}$. For point crossings, the sum of the topological charges of all crossings formed by a given pair of bands needs to be zero, due to a fermion-doubling theorem [26].

- Accidental band crossings are only perturbatively stable. That is, small symmetry-preserving perturbations can move the band crossings in the BZ, but cannot remove them, by opening up a gap. However, large symmetry-preserving deformations can completely remove the band crossings. E.g., for point crossings one can pair annihilate two point crossings with opposite topological charge by a large symmetry-preserving deformation.

It follows from the last point above, that classifications of accidental band crossings based on symmetry and topology only tell us whether for a given set of symmetries a band crossing is *possible*. I.e., these classifications only tell us whether a given set of symmetries protect band crossings or not. They do not tell us whether these crossings actually occur, which depends on the detailed energetics of the bands (i.e., on how the bands disperse through the BZ).

2.1 Classification of band crossings

Topological band crossings of the accidental type can be classified using the Dirac-matrix Hamiltonian method [2, 27, 28]. This method relies on the fact that close to a band crossing the Bloch Hamiltonian $H(\mathbf{k})$, Eq. (1), can in general be approximated by a Dirac Hamiltonian, i.e., by

$$H_D(\mathbf{k}) = \sum_{j=1}^{d} k_j \gamma_j, \tag{3}$$

where d is the spatial dimension and γ_j are gamma matrices obeying the anti-commutation relations

$$\{\gamma_i, \gamma_j\} = 2\delta_{ij}\mathbb{1}, \qquad j = 0, 1, \ldots, d. \tag{4}$$

Using Eq. (4), we find that $H_D^2 = \sum_{j=1}^{d} k_j^2 \mathbb{1}$. Hence, the energy spectrum of $H_D(\mathbf{k})$ is given by

$$E = \pm\sqrt{\sum_{j=1}^{d} k_j^2}, \tag{5}$$

which exhibits a band crossing at $\mathbf{k} = \mathbf{0}$, where the bands become degenerate with $E = 0$. (I.e., the Dirac Hamiltonian has no gap.) The Dirac-matrix Hamiltonian method analyzes the stability of the gapless Dirac-Hamiltonian (3) against gap-opening deformations. That is, one studies whether there exists a gap-opening mass term $m\gamma_0$, i.e., an additional gamma matrix γ_0 with $\{\gamma_0, \gamma_j\} = 0$ ($j = 1, 2, \ldots, d$), with which $H_D(\mathbf{k})$ can be deformed. If such a mass term exists, then the band crossing can be removed. I.e., by adding $m\gamma_0$ to H_D the spectrum deforms into $E = \pm\sqrt{m^2 + \sum_{j=1}^{d} k_j^2}$, which has no band crossing anymore at $\mathbf{k} = 0$. This indicates that the band crossing is topologically trivial. However, if there does not exist an additional gamma matrix γ_0, then the band crossing is topologically nontrivial and stable against deformations.
The classification of band crossings is done in terms of the following three characteristics (cf. Table 1):

(i) Spatial and nonspatial symmetries of the Bloch Hamiltonian $H(\mathbf{k})$.

(ii) The co-dimension $p = d - d_{BC}$ of the band crossing, where d_{BC} is the dimension of the band crossing. (I.e., $d_{BC} = 0$ for point crossings, $d_{BC} = 1$ for line crossings, etc.)

(iii) How the band crossing transforms under the nonspatial (anti-unitary) symmetries, which map $\mathbf{k} \to -\mathbf{k}$. That is, we need to distinguish whether the band crossing is mapped onto itself under the nonspatial symmetries or not, see Fig. 2. For this reason we need to differentiate between band crossings at high-symmetry points and off high-symmetry points of the BZ.

Before performing the classification, let us first discuss how the spatial and nonspatial symmetries restrict the form of the Dirac Hamiltonian (3).

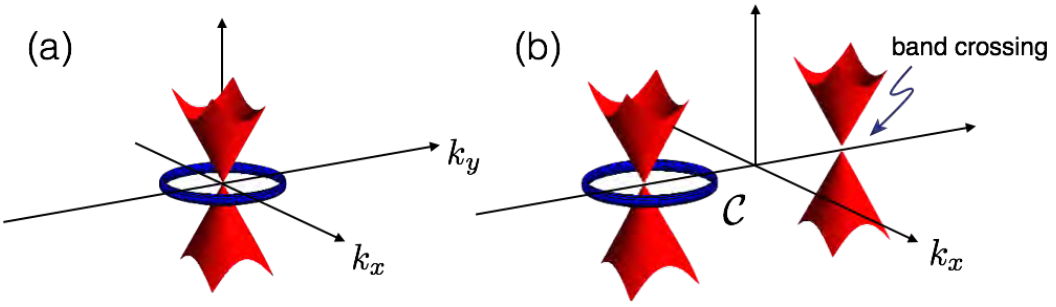

Fig. 2: *The classification of stable band crossings depends on how the band crossings transform under nonspatial (anti-unitary) symmetries. (a) The band crossing is left invariant under nonspatial symmetries. (b) Two band crossings are pairwise related by the nonspatial symmetries, which map* $\mathbf{k} \to -\mathbf{k}$.

2.1.1 Symmetry operations

We consider the classification in terms of both nonspatial and spatial symmetries.

Nonspatial symmetries. Nonspatial symmetries are symmetries that act locally in real space, i.e., they do not transform different lattice sites into each other. There are three different nonspatial symmetries that need to be considered: anti-unitary time-reversal symmetry (TRS) and particle-hole symmetry (PHS), as well as chiral (i.e., sublattice symmetry) [2, 29]. Here, "anti-unitary" refers to the fact that these symmetries can be written as a product of a unitary matrix U with the complex conjugation operator $\mathcal{K}$. In momentum space, time-reversal and particle-hole symmetry act on the Bloch (or Bogoliubov-de Gennes) Hamiltonian as

$$\mathcal{T}^{-1}H(-\mathbf{k})\mathcal{T} = +H(\mathbf{k}), \quad \text{and} \quad \mathcal{C}^{-1}H(-\mathbf{k})\mathcal{C} = -H(\mathbf{k}), \tag{6a}$$

respectively, where $\mathcal{T}$ and $\mathcal{C}$ are the anti-unitary operators for time-reversal and particle-hole symmetry. Both $\mathcal{T}$ and $\mathcal{C}$ can square either to $+1$ or -1, depending on the type of the symmetry (see last three columns of Table 1). Chiral symmetry, on the other hand, is implemented by[2]

$$\mathcal{S}^{-1}H(\mathbf{k})\mathcal{S} = -H(\mathbf{k}), \tag{6b}$$

where $\mathcal{S}$ is a unitary operator. Symmetries (6) define the ten Altland-Zirnbauer (AZ) symmetry classes (i.e., the "ten-fold way") [2, 30, 31], which are listed in Table 1. The first column in Table 1 gives the name of the ten AZ symmetry classes. The labels T, C, and S in the last three columns indicate the presence ("+", "−", and "1") or absence ("0") of time-reversal symmetry, particle-hole symmetry, and chiral symmetry, respectively, as well as the sign of the squared symmetry operators $\mathcal{T}^2$ and $\mathcal{C}^2$.
Combining Eqs. (6) with Eq. (3), we find that when the Dirac Hamiltonian obeys TRS, PHS, or chiral symmetry, the gamma matrices in Eq. (3) must satisfy

$$\{\gamma_i, \mathcal{T}\} = 0, \quad [\gamma_i, \mathcal{C}] = 0, \quad \{\gamma_i, \mathcal{S}\} = 0, \tag{7}$$

[2]Note that combining TRS with PHS yields a chiral symmetry.

Table 1: *Classification of stable band crossings in terms of the ten AZ symmetry classes [2], which are listed in the first column. The first and second rows give the co-dimensions $p = d - d_{BC}$ for band crossings at high-symmetry points [Fig. 2(a)] and away from high-symmetry points of the BZ [Fig. 2(b)], respectively.*

at high-sym. point off high-sym. point	p=8 p=2	p=1 p=3	p=2 p=4	p=3 p=5	p=4 p=6	p=5 p=7	p=6 p=8	p=7 p=1	T	C	S
A	0	$\mathbb{Z}$	0	$\mathbb{Z}$	0	$\mathbb{Z}$	0	$\mathbb{Z}$	0	0	0
AIII	$\mathbb{Z}$	0	$\mathbb{Z}$	0	$\mathbb{Z}$	0	$\mathbb{Z}$	0	0	0	1
AI	0	0[a]	0	$2\mathbb{Z}$	0	$\mathbb{Z}_2$[a,b]	$\mathbb{Z}_2$[b]	$\mathbb{Z}$	+	0	0
BDI	$\mathbb{Z}$	0	0[a]	0	$2\mathbb{Z}$	0	$\mathbb{Z}_2$[a,b]	$\mathbb{Z}_2$[b]	+	+	1
D	$\mathbb{Z}_2$[b]	$\mathbb{Z}$	0	0[a]	0	$2\mathbb{Z}$	0	$\mathbb{Z}_2$[a,b]	0	+	0
DIII	$\mathbb{Z}_2$[a,b]	$\mathbb{Z}_2$[b]	$\mathbb{Z}$	0	0[a]	0	$2\mathbb{Z}$	0	−	+	1
AII	0	$\mathbb{Z}_2$[a,b]	$\mathbb{Z}_2$[b]	$\mathbb{Z}$	0	0[a]	0	$2\mathbb{Z}$	−	0	0
CII	$2\mathbb{Z}$	0	$\mathbb{Z}_2$[a,b]	$\mathbb{Z}_2$[b]	$\mathbb{Z}$	0	0[a]	0	−	−	1
C	0	$2\mathbb{Z}$	0	$\mathbb{Z}_2$[a,b]	$\mathbb{Z}_2$[b]	$\mathbb{Z}$	0	0[a]	0	−	0
CI	0[a]	0	$2\mathbb{Z}$	0	$\mathbb{Z}_2$[a,b]	$\mathbb{Z}_2$[b]	$\mathbb{Z}$	0	+	−	1

[a] For these entries there can exist bulk band crossings away from high-symmetry points that are protected by $\mathbb{Z}$ invariants inherited from classes A and AIII. (TRS or PHS does not trivialize the $\mathbb{Z}$ invariants.)

[b] $\mathbb{Z}_2$ invariants protect only band crossings of dimension zero at high-symmetry points.

where $i = 1, 2, \ldots, d$. Similarly, any mass term $m\gamma_0$ that leads to the opening of a gap at the band crossing must satisfy

$$[\gamma_0, \mathcal{T}] = 0, \quad \{\gamma_0, \mathcal{C}\} = 0, \quad \{\gamma_0, \mathcal{S}\} = 0. \tag{8}$$

Spatial symmetries. Spatial symmetries are symmetries that act non-locally in position space, i.e., they transform different lattice sites into each other. Point-group symmetries are an example of spatial symmetries. Here, we shall focus on reflection symmetries with the unitary operator R. For concreteness we assume that R lets $x \to -x$. The invariance of the Bloch Hamiltonian (1) under this reflection implies

$$R^{-1} H(-k_1, \tilde{\mathbf{k}}) R = H(k_1, \tilde{\mathbf{k}}), \tag{9}$$

where $\tilde{\mathbf{k}} = (k_2, \ldots, k_d)$ and the unitary reflection operator R can only depend on k_1, since it is symmorphic [cf. Eq. (44)]. Note that for spin-$\frac{1}{2}$ particles (e.g., Bloch electrons with spin-orbit coupling) R transforms the spin degree of freedom as

$$R \hat{S}_x R^{-1} = \hat{S}_x \quad \text{and} \quad R \hat{S}_{y,z} R^{-1} = -\hat{S}_{y,z}, \tag{10}$$

where $\hat{S}_i = \frac{\hbar}{2}\hat{\sigma}_i$ is the spin operator. Hence, the spin part of R is given by $i\sigma_x$.[3] In general, R contains also an internal part which rearranges the positions of the atoms in the unit cell.

[3] The reason to include the factor i here is to ensure that $R^2 = -1$, since R^2 effectively corresponds to a spin rotation by 2π. However, in general, there is a phase ambiguity in the definition of R, since a phase can be absorbed in the electronic creation/annihilation operators.

Combining Eq. (9) with Eq. (3), we find that when the Dirac Hamiltonian obeys reflection symmetry, the gamma matrices in Eq. (3) must satisfy

$$\{\gamma_1, R\} = 0, \quad [\gamma_j, R] = 0, \quad \text{where } j = 2, 3, \ldots, d, \tag{11}$$

and the mass term must satisfy $[\gamma_0, R] = 0$.

2.1.2 Band crossings at high-symmetry points

We will now use the Dirac-matrix Hamiltonian method[4] to classify band crossings at high-symmetry points of the BZ, i.e., at time-reversal invariant momenta (TRIMs) of the BZ, e.g., the Γ point. This classification approach consists of the following steps:

1. Write down a d-dimensional gapless Dirac Hamiltonian H_D of the form of Eq. (3), that is invariant under all the considered symmetries. The matrix dimension of the gamma matrices should be minimal, i.e., large enough such that all symmetries can be implemented in a nontrivial way, but not larger.

2. Check whether there exists a symmetry-allowed mass term $m\gamma_0$, which anticommutes with H_D. If *yes*, then the band crossing can be gapped out. This indicates that the band crossing is topologically trivial, which is labeled by "0" in Table 1. If *no*, then the band crossing is topologically stable (i.e., protected by the symmetries), which is labeled by "$\mathbb{Z}$ or "$\mathbb{Z}_2$" in Table 1.

3. To determine whether there is a single or multiple band crossings protected by the symmetries, we have to consider multiple copies of the Dirac Hamiltonian H_D. Doubled versions of H_D can be obtained as

$$H_D^{\text{db}} = \sum_{i \in A} k_i \gamma_i \otimes \sigma_z + \sum_{i \in A^c} k_i \gamma_i \otimes \mathbb{1}, \tag{12}$$

   where the first summation is over an arbitrary subset $A \subseteq \{1, 2, ..., d\}$ and the second summation is over the complement of this subset A^c. We then have to check whether there exist gap-opening terms for these enlarged Dirac Hamiltonians. If there exists a mass term for all possible versions of H_D^{db}, then the band crossing is classified by a $\mathbb{Z}_2$ invariant. If the band crossing is stable for an arbitrary number of copies of H_D, then it is classified by a $\mathbb{Z}$ number, see Table 1.

To make this more explicit, let us discuss some specific cases.

[4] This approach is closely related to the problem of Clifford algebra extensions [2, 28], which puts it on a rigorous footing.

Class A in 2D. First, we consider a band crossing in a two-dimensional system without any symmetries, corresponding to class A in Table 1. The generic low-energy 2×2 Hamiltonian for such a band crossing at $\mathbf{k} = 0$ reads $\mathcal{H}^A_{2D} = \sum_{\mathbf{k}} \Psi^\dagger_{\mathbf{k}} H^A_{2D} \Psi_{\mathbf{k}}$, where

$$H^A_{2D} = k_x\sigma_x + k_y\sigma_y \tag{13}$$

and $\Psi_{\mathbf{k}} = (c_{1\mathbf{k}}, c_{2\mathbf{k}})^T$ is a spinor with two orbital degrees of freedom. Since this band crossing can be gapped out by the mass term $m\sigma_z$, it is topologically trivial and therefore unstable. This is indicated by a "0" in the fourth column of Table 1.

Class A in 3D. Next, we study a zero-dimensional band crossing in three-dimensions without any symmetries. This type of band crossing is realized in Weyl semimetals [2, 5, 6]. The low-energy 2×2 Hamiltonian takes the form $\mathcal{H}^A_{3D} = \sum_{\mathbf{k}} \Psi^\dagger_{\mathbf{k}} H^A_{3D} \Psi_{\mathbf{k}}$, with

$$H^A_{3D} = k_x\sigma_x + k_y\sigma_y + k_z\sigma_z. \tag{14}$$

It is impossible to find a mass term for this Hamiltonian, because there exist only three gamma matrices of rank 2. (There exists no "fourth Pauli matrix" that anticommutes with H^A_{3D}.) Therefore, the band-crossing is stable. To determine whether the Weyl crossing (14) has a $\mathbb{Z}$ or $\mathbb{Z}_2$ classification, we need to consider all possible doubled versions of H^A_{3D}, cf. Eq. (12). We can consider, for example, the following doubled version of H^A_{3D}

$$H^{A,\text{db1}}_{3D} = k_x\sigma_x \otimes \sigma_z + k_y\sigma_y \otimes \sigma_0 + k_z\sigma_z \otimes \sigma_0, \tag{15}$$

where $\otimes$ denotes the tensor product between two Pauli matrices. For this doubled version of H^A_{3D}, there exist two mass terms, e.g., $\sigma_x \otimes \sigma_x$ and $\sigma_x \otimes \sigma_y$, which gap out the band crossing. However, there exists another doubled version of H^A_{3D}, namely

$$H^{A,\text{db2}}_{3D} = k_x\sigma_x \otimes \sigma_0 + k_y\sigma_y \otimes \sigma_0 + k_z\sigma_z \otimes \sigma_0, \tag{16}$$

whose band crossing is stable. We find that there does not exist any mass term for $H^{A,\text{db2}}_{3D}$, which gaps out the band crossing. Since we have found one doubled version of H^A_{3D} which has a stable (four-fold degenerate) band crossing, we conclude that Weyl band crossings exhibit a $\mathbb{Z}$ classification. (One can show that there exist also multiple copies of H^A_{3D} with stable band crossings.) This is indicated by the label "$\mathbb{Z}$" in the fifth column of Table 1.
The Weyl points described by Eq. (14) are monopoles of Berry flux, i.e., they realize hedgehog defects of the Berry curvature (see Fig. 4). The stability of these Weyl points is guaranteed by a quantized Chern number (see Sec. 2.2).

Class A + R in 2D. Let us now add reflection symmetry to the game. We consider again a two-orbital system with the low-energy Hamiltonian $\mathcal{H}^{A+R}_{2D} = \sum_{\mathbf{k}} \Psi^\dagger_{\mathbf{k}} H^{A+R}_{2D} \Psi_{\mathbf{k}}$, where

$$H^{A+R}_{2D} = k_x\sigma_x + k_y\sigma_y, \tag{17}$$

which is symmetric under reflection symmetry $R^{-1}H_{2D}^{A+R}(-k_x,k_y)R = H_{2D}^{A+R}(k_x,k_y)$, with $R=\sigma_y$. This Hamiltonian describes the low-energy physics of a single Dirac cone of graphene. We observe that the only possible gap-opening mass term $m\sigma_z$, which anticommutes with H_{2D}^{A+R}, is symmetry forbidden, since it breaks reflections symmetry ($R^{-1}\sigma_z R=-\sigma_z$). Hence, the band-crossing of H_{2D}^{A+R} at $\mathbf{k}=0$ is stable and protected by reflection symmetry. We find that also the doubled version of H_{2D}^{A+R},

$$H_{2D}^{A+R,\text{db}} = k_x\sigma_x\otimes\sigma_0 + k_y\sigma_y\otimes\sigma_0, \tag{18}$$

is stable, since there exists no reflection-symmetric mass term. For example, $\hat{m}=\sigma_z\otimes\sigma_x$ breaks reflection, since $(\sigma_y\otimes\sigma_0)^{-1}\hat{m}(\sigma_y\otimes\sigma_0)\neq\hat{m}$. Therefore, the reflection-symmetric band crossing (17) has a $\mathbb{Z}$ classification. This is indicated by the label "$M\mathbb{Z}$" in the fifth column of Table VIII of Ref. [2].

Class AII in 2D. Next, we study a band crossing in two-dimensions with time-reversal symmetry ($\mathcal{T}^2=-1$), corresponding to class AII in Table 1. The low-energy Dirac Hamiltonian reads again

$$H_{2D}^{\text{AII}} = k_x\sigma_x + k_y\sigma_y. \tag{19}$$

But now we impose time-reversal symmetry (6a) with the operator $\mathcal{T}=i\sigma_y\mathcal{K}$, which squares to -1 (class AII). This type of time-reversal symmetric band crossing is realized at the surface of three-dimensional topological insulators with spin-orbit coupling. The only possible mass term, which anticommutes with H_{2D}^{AII}, is $m\sigma_z$. However, $m\sigma_z$ breaks time-reversal symmetry (since, $\mathcal{T}^{-1}m\sigma_z\mathcal{T}\neq m\sigma_z$) and is therefore forbidden by symmetry. Hence, Eq. (19) describes a topologically stable band crossing in class AII. Next, we examine different doubled versions of H_{2D}^{AII}, i.e.,

$$H_{2D}^{\text{AII,db}} = \begin{pmatrix} H_{2D}^{\text{AII}} & 0 \\ 0 & H_{2D}^{\text{AII}'} \end{pmatrix}, \tag{20}$$

where $H_{2D}^{\text{AII}'}\in\{\pm k_x\sigma_x\pm k_y\sigma_y, \pm k_x\sigma_x\mp k_y\sigma_y\}$, see Eq. (12). (The time-reversal operator for these double Hamiltonians is $\mathcal{T}=i\sigma_y\otimes\sigma_0\mathcal{K}$.) It is not difficult to show that for each of the four versions of $H_{2D}^{\text{AII,db}}$ there exists at least one symmetry-preserving mass term, which gaps out the band crossing. For example, for the first version of $H_{2D}^{\text{AII,db}}$ with $H_{2D}^{\text{AII}'}=+k_x\sigma_x+k_y\sigma_y$, the mass term is $\sigma_z\otimes\sigma_y$. Thus, the band crossings described by $H_{2D}^{\text{AII,db}}$ is unstable. Therefore, we conclude that Eq. (19) has a $\mathbb{Z}_2$ classification, see fourth column of Table 1.

2.1.3 Band crossings off high-symmetry points

In this section we classify band crossings that are located away from high-symmetry points, i.e., away from the TRIMs of the BZ, see Fig. 2(b). These band crossings can be moved around in the BZ, as they are not pinned at the TRIMs. They transform pairwise into each other by the

nonspatial anti-unitary symmetries (time-reversal and particle-hole symmetry). For this reason, we have to take into account the full momentum dependence of the Hamiltonian in the entire BZ. That is, within the Dirac-matrix Hamiltonian approach, we need to consider the following type of Hamiltonian [27]

$$H_D = \sum_{i=1}^{p-1} \sin k_i \gamma_i + \Big(p - 1 - \sum_{i=1}^{p} \cos k_i\Big)\tilde{\gamma}_0, \tag{21}$$

which contains the momentum-dependent mass term $\tilde{\gamma}_0$, cf. Eq. (3). The Dirac Hamiltonian (21) describes d_{BC}-dimensional band crossings (with $d_{BC} = d - p$), which are located at

$$\mathbf{k} = (0, \ldots, 0, \pm\pi/2, k_{p+1}, \ldots, k_d). \tag{22}$$

We observe that the band crossings (22) are located away from the high-symmetry points $(0, 0, 0, \ldots, 0)$, $(\pi, 0, 0, \ldots, 0)$, $(0, \pi, 0, \ldots, 0)$, etc. of the BZ. The classification of these band crossings proceeds in a similar way as in Sec. 2.1.2. It consists of the following steps:

1. Write down a d-dimensional Dirac Hamiltonian H_D of the form Eq. (21) with $p{=}d{-}d_{BC}$, which satisfies all the considered symmetries. The rank of the gamma matrices in Eq. (21) should be large enough, such that all symmetries can be implemented in a nontrivial way, but not larger.

2. Check, whether

   - there exists an additional momentum-independent mass term $\tilde{\Gamma}$, which anticommutes with H_D and which is invariant under all symmetries.
   - there exists an additional momentum-dependent kinetic term $\sin k_p \gamma_p$, which anticommutes with H_D and which respects all symmetries.

   If the answer is *yes* for either of the above two points, then the band crossing can be gapped out. Hence, the band crossing is topologically trivial (entries labeled by "0" in Table 1). If the answer is *no* for both of the above points, then the band crossing is topologically stable (entries labeled by "$\mathbb{Z}$" or "$\mathbb{Z}_2$" in Table 1).

3. To determine whether there is a single or multiple band crossings protected by the symmetries, consider multiple copies of H_D, similar to Eq. (12).

Using this approach it was shown that only $\mathbb{Z}$-type invariants can ensure the stability of band-crossings off high-symmetry points [2]. ($\mathbb{Z}_2$-type invariants do not give rise to stable band crossings off high-symmetry points.) To exemplify this, we discuss some specific cases.

2.2 Weyl semimetal

We study the band crossing points of a three-dimensional Weyl semimetal [2, 5, 6], which belongs to symmetry class A (cf. Sec. 2.1.2). The Hamiltonian is defined on the cubic lattice and is given by $\mathcal{H}^A_{3D} = \sum_{\mathbf{k}} \Psi_{\mathbf{k}} H^A_{3D} \Psi_{\mathbf{k}}$, with (cf. Eq. (21) with $p = 3$)[5]

$$H^A_{3D} = \sin k_x \sigma_x + \sin k_y \sigma_y + (2 - \cos k_x - \cos k_y - \cos k_z)\sigma_z, \tag{23}$$

and the spinor $\Psi_{\mathbf{k}} = (c_{1\mathbf{k}}, c_{2\mathbf{k}})$, which has two orbital degrees of freedom (e.g., s and p orbitals), but no spin-degree of freedom, since the semimetal is assumed to be magnetically ordered. The spectrum of Eq. (23) is given by

$$E_{\mathbf{k}} = \pm\sqrt{(\sin k_x)^2 + (\sin k_y)^2 + (2 - \cos k_x - \cos k_y - \cos k_z)^2}. \tag{24}$$

H^A_{3D} exhibits two band crossing points at $E = 0$ (called Weyl points), which are located at $(0, 0, \pm\pi/2)$. As in Sec. 2.1.2, we find that these Weyl nodes are topologically stable, since there does not exist any fourth gamma matrix of rank two. (I.e., there exist no additional mass or kinetic terms.) We also find that the doubled version $H^A_{3D} \otimes \sigma_0$ has stable band crossings. Hence, the classification is of $\mathbb{Z}$ type, see third column of Table 1.

The stability of the Weyl points is guaranteed by a quantized Chern number

$$C = \frac{1}{2\pi} \oint_{\mathcal{C}} \mathcal{F}(\mathbf{k}) d\mathbf{k}, \qquad \text{where} \qquad \mathcal{F}(\mathbf{k}) = \nabla_{\mathbf{k}} \times \mathbf{A}_{\mathbf{k}} \tag{25}$$

is the Berry curvature of the occupied band and $\mathcal{C}$ is a two-dimensional closed integration contour. The Berry connection $\mathbf{A}_{\mathbf{k}}$ is defined as $\mathbf{A}_{\mathbf{k}} = i\langle u_-(\mathbf{k})|\nabla_{\mathbf{k}}|u_-(\mathbf{k})\rangle$, with $|u_-(\mathbf{k})\rangle$ the Bloch state of the occupied band. The Weyl points act as sources and drains of Berry curvature, i.e., the vector field $\mathcal{F}(\mathbf{k})$ points inwards at one Weyl point and outwards at the other. The Chern number (25) measures how much Berry flux passes through the contour $\mathcal{C}$. For contours that enclose one of the two Weyl points the Chern number is $C = \pm 1$. For contours that do not enclose a Weyl point, the Chern number is zero $C = 0$.

For Hamiltonian (23) the Chern number can be rewritten in the simple form[6]

$$C(k_z) = \frac{1}{4\pi} \oint_{\mathcal{C}_{k_z}} dk_x dk_y \, \hat{\mathbf{d}}_{\mathbf{k}} \cdot \left[\partial_{k_x} \hat{\mathbf{d}}_{\mathbf{k}} \times \partial_{k_y} \hat{\mathbf{d}}_{\mathbf{k}}\right], \qquad \text{with} \quad \hat{\mathbf{d}}_{\mathbf{k}} = \frac{\mathbf{d}(\mathbf{k})}{|\mathbf{d}(\mathbf{k})|}, \tag{26}$$

and $d_x(\mathbf{k}) = \sin k_x$, $d_y(\mathbf{k}) = \sin k_y$, and $d_z(\mathbf{k}) = (2 - \cos k_x - \cos k_y - \cos k_z)$. Here, for simplicity, we choose $\mathcal{C}$ to be parallel to the $k_x k_y$-plane, see Fig. 4(a). The vector $\hat{\mathbf{d}}_{\mathbf{k}}$ in Eq. (26) defines a map from $\mathbf{k}$ to the unit sphere S^2, see Figs. 3(a) and 3(b). The Chern number $C(k_z)$, Eq. (26), measures how many times the $\hat{\mathbf{d}}_{\mathbf{k}}$-vector wraps around S^2 as $\mathbf{k}$ sweeps through the contour $\mathcal{C}_{k_z}$. (Note that for $\mathbf{k}$ restricted to a spherical contour $\mathcal{C}$, $\hat{\mathbf{d}}_{\mathbf{k}}$ represents a map from S^2 to S^2, whose topology is given by the second homotopy group $\pi_2(S^2) = \mathbb{Z}$ [32].) Let us now study how $C(k_z)$, Eq. (26), changes as a function of k_z. Two different regions of k_z can be distinguished:

[5]Note that this model has an inversion symmetry, i.e., $(\sigma_z)^{-1} H^A_{3D}(-\mathbf{k})\sigma_z = H^A_{3D}(\mathbf{k})$, which ensures that the two Weyl points are at the same energy.

[6]The fact that there is a non-zero Chern number can also be diagnosed from the parity eigenvalues at the TRIMs [5]. The parity eigenvalues at the Γ point are opposite to those at all the other TRIMs. From this it follows that the Chern number $C(k_z = 0)$ must be non-zero.

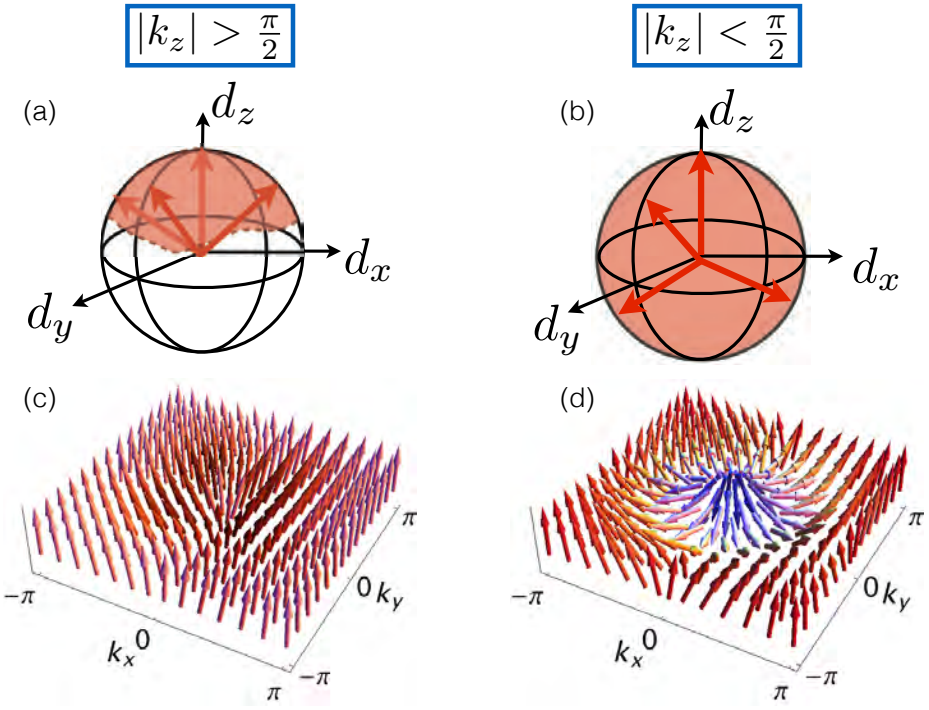

Fig. 3: *(a),(b) show the regions covered by the* $\mathbf{d_k}$*-vector, Eq.* (26)*, on the unit sphere. (c), (d) depict the textures of* $\mathbf{d_k}$ *in the* k_xk_y*-plane, i.e., in the contour* $\mathcal{C}_{k_z}$*. (a), (c) corresponds to* $C(k_z) = 0$*, while (b), (d) represents* $C(k_z) \neq 0$*.*

Trivial region. For $|k_z| > \pi/2$, the $\hat{\mathbf{d}}_\mathbf{k}$-vector covers only a small region around the north pole of S^2, i.e., it points mostly upwards. Hence, $\hat{\mathbf{d}}_\mathbf{k}$ does not wrap around S^2, leading to a zero Chern number $C(k_z) = 0$, see left-hand side of Fig. 3. This follows also from the fact that the contour $\mathcal{C}$ can be continuously shrunk to zero, without crossing through the singularities of the Weyl points. Thus, the integral (26) must vanish.

Topological region. For $|k_z| < \pi/2$, however, the $\hat{\mathbf{d}}_\mathbf{k}$-vector wraps once around the unit sphere S^2. That is, it points along all directions as $\mathbf{k}$ sweeps through $\mathcal{C}_{k_z}$, producing a Skyrmion texture in the k_xk_y-plane, see right-hand side of Fig. 3. As a consequence, the Chern number is nonzero, i.e., $C(k_z) = \pm 1$, which endows the Weyl points with a nonzero topological charge (also know as "chirality"). This agrees with the fact that the contour $\mathcal{C}$ cannot be continuously shrunk to zero, without crossing through the Weyl point singularities. Hence, the integral (26) must be nonzero.

Due to the periodicity of the BZ, we can consider the contour $\mathcal{C}_{k_z}$ to enclose either the upper or the lower part of the BZ, see Fig. 4(a). Both ways of closing the contour must give consistent results. A contour $\mathcal{C}_{k_z}$ with $|k_z| > \pi/2$, which can be shrunk to zero, can also be viewed as enclosing both Weyl points. Hence, the Chern numbers of the two Weyl points must add up to zero, i.e., they must have opposite topological charges, which is a manifestation of the fermion-doubling theorem [26].

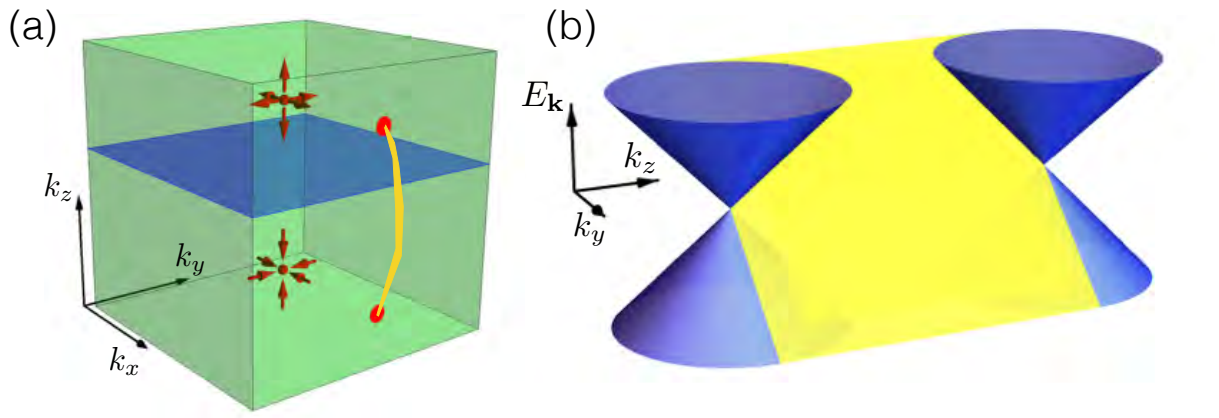

Fig. 4: *(a) The Weyl points (red spheres) are sources and drains of Berry flux (red arrows). In the surface BZ there exists a Fermi arc state (yellow), which connects the projection of the two Weyl points. The blue plane indicates the integration contour $\mathcal{C}_{k_z}$ of Eq.* (26)*. (b) Schematic energy dispersion of the Fermi arc state in the (100) surface BZ. The Fermi arc surface state (yellow) smoothly connects to the linearly dispersing bulk bands (blue) of the two Weyl points.*

2.2.1 Fermi arc surface states

We now discuss the surface states of Weyl semimetals, which arise due to the nontrivial topology of the Weyl points. For this we consider again Hamiltonian (23) restricted to a planar contour $\mathcal{C}_{k_z}$ which is perpendicular to the k_z axis [blue plane in Fig. 4(a)]. As we have seen above, for any contour $\mathcal{C}_{k_z}$ with $|k_z| < \pi/2$ the Chern number is $C = \pm 1$. Thus, each of the two-dimensional Hamiltonians $H^A_{3D,k_z}(k_x, k_y)$,with $|k_z| < \pi/2$, represents a two-dimensional Chern insulator. These Chern insulators all have chiral edge modes, which on the surface perpendicular to, e.g., the x direction, have a linear dispersion with $E \simeq vk_y$. Hence, there is a collection of chiral edge modes on the (100) surface, which all disperse in the same direction. They form an arc in the surface BZ, connecting the projection of the two Weyl points (yellow arc in Fig. 4). This arc smoothly connects to the bulk bands, as shown in Fig. 4(b). We note that these arc states cannot exist in purely two-dimensional systems, as they would contradict the continuity of the band structure (bands cannot terminate at a point). At surfaces, however, these arc states are allowed, since their end points smoothly connect with the bulk bands.

2.2.2 The chiral anomaly

Since the two Weyl points of opposite Chern number (i.e., opposite chirality) are separated by a large momentum in the BZ, one might naively expect that the number of electrons $n_\pm$ at each Weyl point with $C = \pm 1$ are separately conserved. In other words, one might think that besides the regular electric charge $e(n_+ + n_-)$, also the chiral charge $e(n_+ - n_-)$ is conserved. Indeed, within a classical low-energy description of Weyl semimetals the chiral charge is preserved. However, at the quantum level this symmetry is broken, giving rise to an anomaly, i.e., the chiral anomaly [5, 6]. That is, in the presence of electric fields $\mathbf{E}$ and magnetic fields $\mathbf{B}$ the

number of electrons $n_\pm$ at a given Weyl point is changed as

$$\frac{d}{dt}n_\pm = \pm\frac{e^2}{h^2}\mathbf{E}\cdot\mathbf{B}. \tag{27}$$

Therefore, an electric field together with a magnetic field can generate (or destroy) chiral charge, i.e., they can pump electric charges from one Weyl point to the other, leading to valley polarizations. The total electric charge, however, remains preserved in this process. The chiral anomaly has a number of experimental consequences, such as anomalous Hall effect and negative magnetoresistance [6].

2.3 Dirac nodal-line semimetal

As a second example, we study a nodal-line band crossing in a three-dimensional semimetal with time-reversal symmetry (class AI) and reflection symmetry [33, 35, 36]. The Hamiltonian is defined on the cubic lattice and is given by $\mathcal{H}_{3D}^{AI+R} = \sum_{\mathbf{k}} \Psi_{\mathbf{k}}^\dagger H_{3D}^{AI+R}\Psi_{\mathbf{k}}$, where the spinor $\Psi_{\mathbf{k}} = (c_{p\mathbf{k}}, c_{d\mathbf{k}})^T$ describes spinless Bloch electrons (no spin-orbit coupling) originating from p and d orbitals and H_{3D}^{AI+R} reads (cf. Eq. (21) with $p = 2$)[7]

$$H_{3D}^{AI+R} = \sin k_z\sigma_2 + [2 - \cos k_x - \cos k_y - \cos k_z]\,\sigma_3. \tag{28}$$

The spectrum of this Hamiltonian

$$E_{\mathbf{k}} = \pm\lambda_{\mathbf{k}} = \pm\sqrt{(2 - \cos k_x - \cos k_y - \cos k_z)^2 + (\sin k_z)^2}, \tag{29}$$

exhibits a band-crossing at $E = 0$, which is located along a nodal ring within the $k_z = 0$ plane, see Fig. 5(a). Such a nodal-line band crossing at the Fermi energy is realized in Ca_3P_2, CaAgP, and other materials [2,15,33]. Eq. (28) is time-reversal symmetric with the time-reversal operator $\mathcal{T} = \sigma_0\mathcal{K}$, and reflection symmetric, $R^{-1}H_{3D}^{AI+R}(k_x, k_y, -k_z)R = H_{3D}^{AI+R}(k_x, k_y, k_z)$, with the reflection operator $R = \sigma_z$. There is also an inversion symmetry, $\mathcal{P}^{-1}H_{3D}^{AI+R}(-\mathbf{k})\mathcal{P} = H_{3D}^{AI+R}(\mathbf{k})$, with the inversion operator $\mathcal{P} = \sigma_z$. We observe that the only possible mass term $m\tau_x$ that anticommutes with H_{3D}^{AI+R} is symmetry forbidden, since it breaks reflection symmetry ($R^{-1}m\sigma_x R = -m\sigma_x$) and space-time inversion symmetry [$(\mathcal{TP})^{-1}m\sigma_x(\mathcal{TP}) = -m\sigma_x$]. Hence, the nodal line band crossing is stable and protected by reflection symmetry and $\mathcal{PT}$ symmetry. However, the band crossing of the doubled version of H_{3D}^{AI+R}

$$H_{3D}^{AI+R,\mathrm{db}} = \sin k_z\sigma_2 \otimes \sigma_0 + [2 - \cos k_x - \cos k_y - \cos k_z]\,\sigma_3 \otimes \sigma_0. \tag{30}$$

is protected only by reflection but not by $\mathcal{PT}$ symmetry, since the mass term $\hat{m} = \sigma_x \otimes \sigma_y$ is symmetric under $\mathcal{PT}$ [$(\sigma_z\otimes\sigma_0\mathcal{K})^{-1}\hat{m}(\sigma_z\otimes\sigma_0\mathcal{K}) = \hat{m}$], but breaks R [$(\sigma_z\otimes\sigma_0)^{-1}\hat{m}(\sigma_z\otimes\sigma_0) \neq \hat{m}$]. From this we conclude that nodal rings of type (28) have a $\mathbb{Z}$ classification in the presence of reflection symmetry, but only a $\mathbb{Z}_2$ classification in the presence of $\mathcal{PT}$ symmetry.

[7] Here, we have included both $\cos k_x$ and $\cos k_y$ terms in order to deform the nodal line of Eq. (21) into a nodal ring.

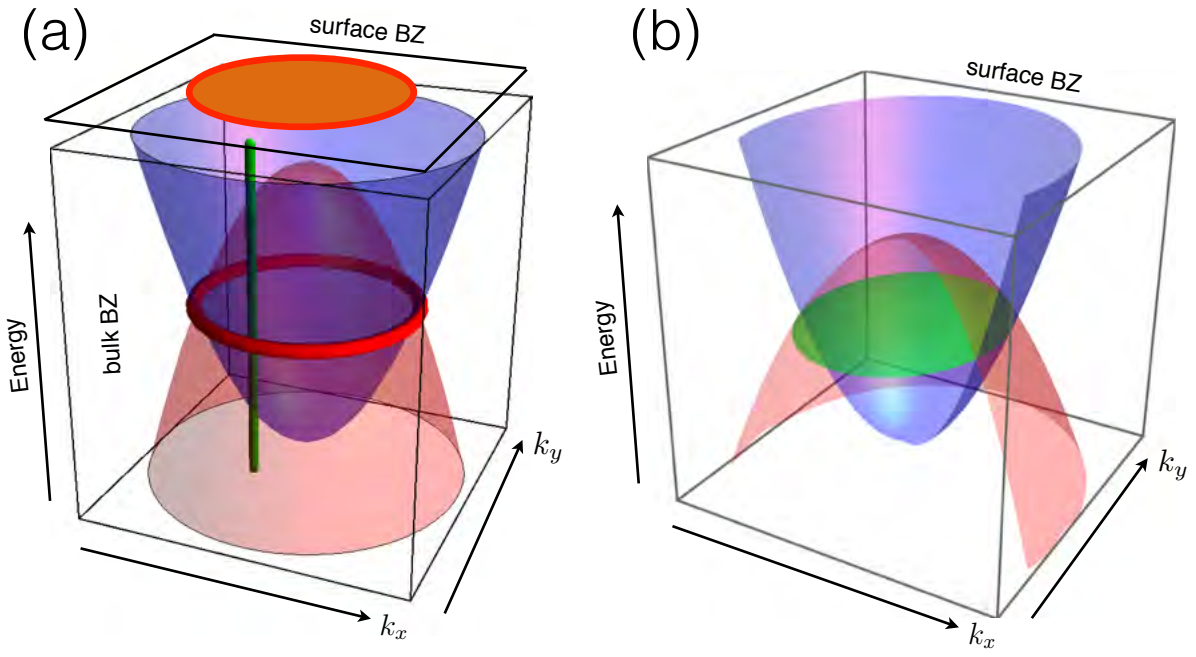

Fig. 5: *(a) Hamiltonian* (28) *describes an electron- and a hole-like band, which cross each other along a nodal loop (red ring). The green line represents the contour $\mathcal{L}$ of Eq.* (31)*. The red area in the surface BZ indicates the region where surface states exist. (b) Schematic energy dispersion of the drumhead surface state in the (001) surface BZ. The drumhead surface state (green) smoothly connects to the bulk bands (blue and red) of the nodal ring.*

The topological invariant, which guarantees the stability of the nodal ring, is the Berry phase. The Berry phase is defined as a one-dimensional contour integral over the Berry connection (for a related mirror invariant, see Ref. [33])

$$P_{\mathcal{L}} = -i \oint_{\mathcal{L}} dk_l \, \langle u_-(\mathbf{k})| \, \nabla_{k_l} \, |u_-(\mathbf{k})\rangle \, . \tag{31}$$

Here, $|u_-(\mathbf{k})\rangle$ is the filled Bloch eigenstate of Eq. (28), which is given by

$$|u_-(\mathbf{k})\rangle = \frac{1}{\sqrt{2\lambda_{\mathbf{k}}(\lambda_{\mathbf{k}} - M_{\mathbf{k}})}} \begin{pmatrix} \lambda_{\mathbf{k}} - M_{\mathbf{k}} \\ i \sin k_z \end{pmatrix} , \tag{32}$$

with $M_{\mathbf{k}} = 2 - \cos k_x - \cos k_y - \cos k_z$. Note that the Berry phase is only defined up to mod 2π. One can show that reflection symmetry R and space-time inversion $\mathcal{PT}$ lead to the quantization of the Berry phase, i.e., $P_{\mathcal{L}} \in \{0, \pi\}$ [33]. For contours $\mathcal{L}$ that do not interlink with the nodal ring, the Berry phase (31) is zero, since the contour can be continuously shrunk to a single point. For a contour $\mathcal{L}$ that does interlink with the nodal ring the Berry phase evaluates to $P_{\mathcal{L}} = \pi$. In this case, the contour cannot be continuously shrunk to zero without crossing the nodal ring. Hence, the nodal ring is stable to small changes in the parameters, as long as mirror or $\mathcal{PT}$ symmetry is not broken.

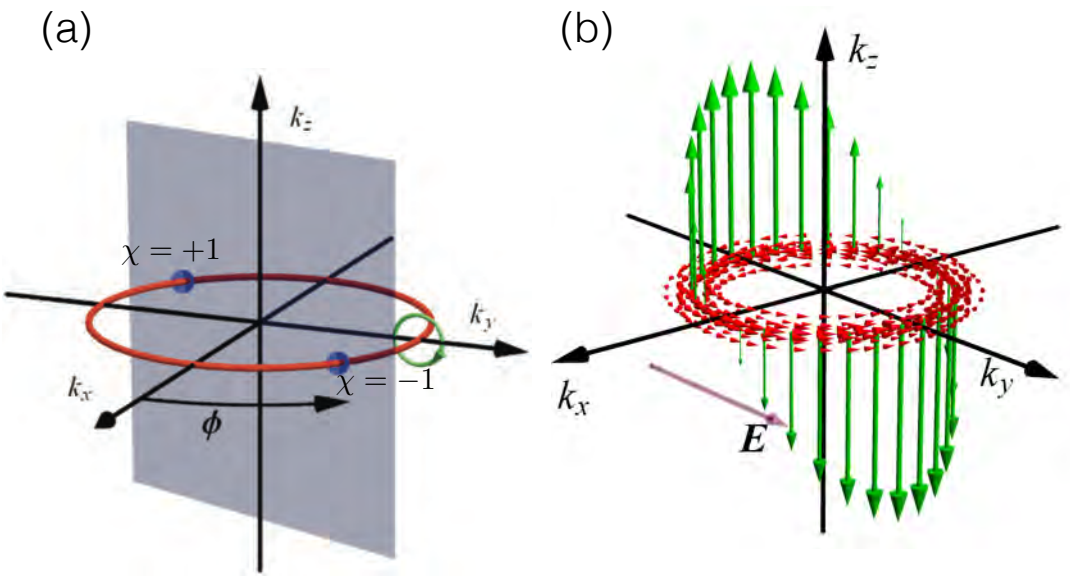

Fig. 6: *(a) The nodal-line semimetal is decomposed into a family of two-dimensional subsystems (blue plane) parametrized by the angle ϕ. (b) In the presence of an electric field (violet arrow), the nonzero Berry curvature (red arrows) leads to a transverse Hall current (green arrows). Figures adapted from Ref. [35].*

2.3.1 Drumhead surface state

We now discuss the surface states of nodal-line semimetals, that arise due to the nontrivial topology of the nodal ring. For this purpose we consider Hamiltonian (28) restricted to a line contour $\mathcal{L}_{k_x,k_y}$, which is perpendicular to the k_xk_y-plane, i.e., along the k_z direction [green line in Fig. 5(a)]. As we have seen above, for any contour $\mathcal{L}_{k_x,k_y}$, with $\cos k_x + \cos k_y > 1$, the Berry phase is $P = \pi$. Hence, each of the one-dimensional Hamiltonians $H^{AI+R}_{3D;k_x,k_y}(k_z)$, with $\cos k_x + \cos k_y > 1$, represents a one-dimensional topological insulator with non-zero Berry phase. These one-dimensional topological insulators all have midgap end states [34]. As a consequence, there is a collection of end states on the (001) surface, which form a drumhead that smoothly connects to the projected bulk bands [green area in Fig. 5(b)]. This drumhead state is not allowed to exist in purely two-dimensional systems, as it would violated the continuity of the band structure (bands cannot terminate at lines). At a surface, however, such drumhead states can exist, since their edges smoothly connect to the bulk bands.

2.3.2 The parity anomaly

To discuss the parity anomaly, we divide the nodal-line semimetal into a collection of two-dimensional subsystems parametrized by the angle $\phi \in [0, \pi)$, as shown in Fig. 6(a). Each of these subsystems contains two Dirac points with opposite sign of Berry phase $\chi = \mathrm{sgn}(P)$, which are related by time-reversal symmetry. The quantum field theory of a single Dirac point

of such a subsystem coupled to an electromagnetic field A_μ includes the term

$$S_{\text{CS}}^{\phi,\chi} = \chi \frac{e^2}{4\pi} \int d^2x dt\, \epsilon^{\mu\nu\lambda} A_\mu \partial_\nu A_\lambda. \tag{33}$$

This Chern-Simons term only arises at the quantum level and is a manifestation of the parity anomaly, since it breaks $\mathcal{PT}$ symmetry. Varying the Chern-Simons term with respect to A_μ, gives the anomalous transverse current

$$j_\mu^{\phi,\chi} = \chi \frac{e^2}{4\pi} \epsilon^{\mu\nu\lambda} \partial_\nu A_\lambda \tag{34}$$

for a single Dirac point in subsystem ϕ with chirality χ. Hence, electromagnetic fields generate a topological current, which flows perpendicular to the applied field. These transverse currents are depicted in green in Fig. 6. For a field along the k_y axis, the transverse currents flow downward on the side of the ring with $k_y > 0$, while they flow upward on the opposite side. This leads to an accumulation of charge on opposite surfaces of nodal-line semimetals. Since the contributions on opposite sides of the nodal ring cancel out, the topological currents can only be measured by a device that filters electrons based on their momenta [35]. Alternatively, the topological currents can be induced and probed by axial gauge fields, which couple oppositely to electrons with opposite momenta [36].

3 Symmetry-enforced band crossings

In this section we study symmetry-enforced band crossings that are *movable* (but not removable) [16–22]. These movable band crossings, which are required to exist by symmetry alone, exhibit the following properties:

- They are protected by nonsymmorphic crystal symmetries, possibly together with non-spatial symmetries. A nonsymmorphic symmetry is a symmetry $G = \{g, \mathbf{t}\}$, which combines a point-group symmetry g with a translation $\mathbf{t}$ by a fraction of a Bravais lattice vector (see Sec. 3.1).

- Symmetry-enforced band crossings are characterized by a global topological charge, which measures the winding of the eigenvalue of G as we go through the BZ. As shown in Fig. 7, one needs to go twice (or n times) through the BZ in order to get back to the same eigenvalue.

- Symmetry-enforced band crossings are globally stable. That is, they cannot be removed, even by large symmetry-preserving deformations. They are required to exist by symmetry alone, independent of any other material details (e.g, chemical composition or energetics of the bands).

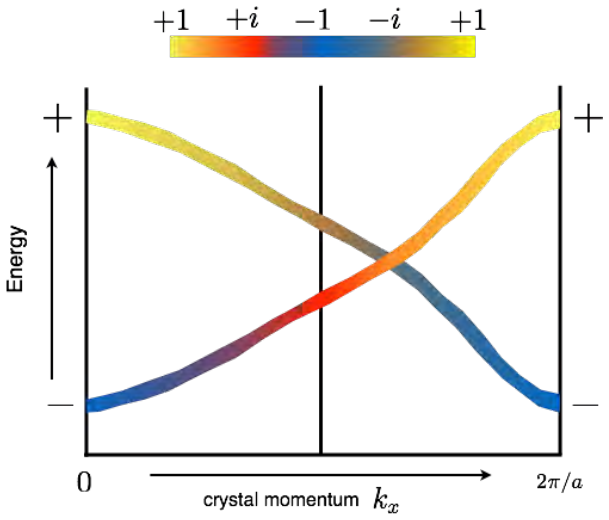

Fig. 7: *Nonsymmorphic symmetries lead to symmetry-enforced band crossings. The color shading indicates how the eigenvalue of the nonsymmorphic symmetry changes as a function of crystal momentum. Note that one needs to go through the BZ twice (or n times), in order to get back to the same eigenvalue.*

Strategy for materials discovery. The last point above allows us to construct the following strategy to discover new materials with topological band crossings [21, 22], which consists of three steps:

(i) First, we identify the space groups (SGs) whose nonsymmorphic symmetries enforce the desired band crossings. This can be done by either (i) computing the algebraic relations obeyed by the symmetry operators or (ii) by computing the compatibility relations between irreducible symmetry representations (irreps).

(ii) Second, we perform a database search for materials in these SGs. The most comprehensive database on inorganic crystals is the Inorganic Crystal Structure Database (ICSD) from the Leibniz Institute in Karlsruhe (https://icsd.fiz-karlsruhe.de). Other databases, which also contain band structures, are the AFLOW database (http://aflowlib.org), the Materials Project database (https://www.materialsproject.org), the database for material sciences at the IOP of the Chinese Academy of Science (http://materiae.iphy.ac.cn), and the Topological Materials Database (https://topologicalquantumchemistry.com).

(iii) Third, we compute the electronic band structure of these materials to check whether the band crossings are near the Fermi energy.

In Secs. 3.2.3 and 3.3.2 we will present two materials that have been found using the above strategy.

3.1 Nonsymmorphic symmetries lead to enforced band crossings

Nonsymmorphic symmetries $G = \{g|\mathbf{t}\}$ combine a point-group symmetry g with a translation $\mathbf{t}$ by a fraction of a Bravais lattice vector, see Fig. 8. Without loss of generality, we can assume

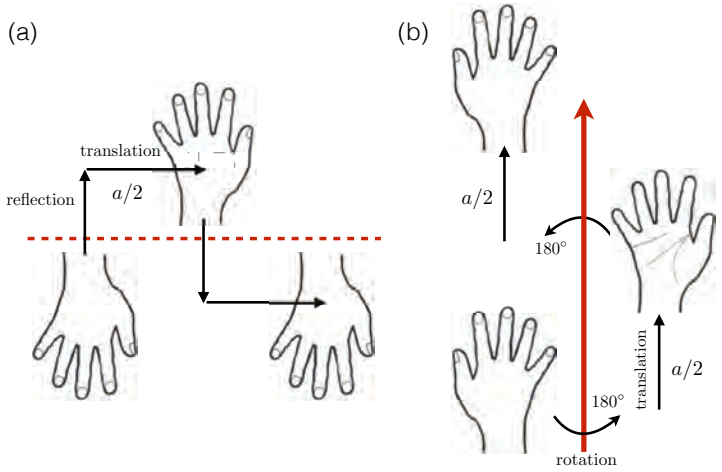

Fig. 8: *This figure illustrates two nonsymmorphic symmetries: A glide reflection in panel (a) and a two-fold screw rotation in panel (b).*

that the fractional translation $\mathbf{t}$ is parallel to the invariant space of g, i.e., that $g\mathbf{t} = \mathbf{t}$. The reason for this is that any component of $\mathbf{t}$ that is not invariant under g can be removed by a suitable choice of unit cell (i.e., a suitable choice of reference for g). (An exception to this rule will be discussed in Sec. 3.3.) Applying an n-fold nonsymmorphic symmetry n times yields a translation, i.e.,

$$G^n = \{g^n|n\mathbf{t}\} = \pm p\, T_{\mathbf{a}}, \quad p \in \{1, 2, \ldots, n-1\}, \tag{35}$$

where $T_{\mathbf{a}}$ is the translation operator for the Bravais lattice vector $\mathbf{a}$ and g is an n-fold point-group symmetry. The $\pm$ sign on the right-hand side of Eq. (35) originates from g^n, which equals -1 for spin-1/2 quasiparticles (Bloch electrons with spin-orbit coupling) and $+1$ for spinless quasiparticles (Bloch electrons without spin-orbit coupling). Two simple examples of nonsymmorphic symmetries are illustrated in Fig. 8:

- a glide reflection $M = \{m|\mathbf{t}\}$, with $M^2 = \pm T_{\mathbf{a}}$
- a two-fold screw rotation $C_2 = \{c_n|\mathbf{t}\}$, with $(C_2)^2 = \pm T_{\mathbf{a}}$

In the band structure of materials with nonsymmorphic symmetries, the operators $G = \{g|\mathbf{t}\}$ can enforce band degeneracies in the g-invariant space of the BZ, i.e., on lines or planes which satisfy $g\mathbf{k} = \mathbf{k}$. In these g-invariant spaces, the Bloch states $|u_m(\mathbf{k})\rangle$ can be constructed in such a way that they are simultaneous eigenfunctions of both G and the Hamiltonian. To derive the G-eigenvalues of the Bloch states $|u_m(\mathbf{k})\rangle$, we observe that

$$G^n = \pm e^{-ip\mathbf{k}\cdot\mathbf{a}}, \tag{36}$$

which follows from Eq. (35). Hence, the eigenvalues of G are

$$G\,|\psi_m(\mathbf{k})\rangle = \begin{cases} e^{i\pi(2m+1)/n} e^{-ip\mathbf{k}\cdot\mathbf{a}/n}\,|\psi_m(\mathbf{k})\rangle\,, & \text{for spin 1/2,} \\ e^{i2\pi m/n}\, e^{-ip\mathbf{k}\cdot\mathbf{a}/n}\,|\psi_m(\mathbf{k})\rangle\,, & \text{for spin 0,} \end{cases} \tag{37}$$

where $m \in \{0, 1, \ldots, n-1\}$. Because of the phase factor $e^{-ip\mathbf{k}\cdot\mathbf{a}/n}$ in Eq. (37) the eigensectors of G can switch, as $\mathbf{k}$ moves along the g-invariant space. From this it follows that pairs of bands must cross at least once within the invariant space.[8] With this we have found the basic mechanism that leads to symmetry-enforced band degeneracies [16–19],

Let us now explain in more detail how a screw rotation leads to a symmetry-enforced band crossing in a simple one-dimensional system with two atoms per unit cell. In momentum space such a system is described by a two-band Hamiltonian $\mathcal{H}(k)$. The screw rotation symmetry (π rotation, followed by half translation) takes the form [16]

$$G(k)\mathcal{H}(k)G^{-1}(k) = \mathcal{H}(k), \qquad G(k) = \begin{pmatrix} 0 & e^{-ik} \\ 1 & 0 \end{pmatrix}, \tag{38}$$

where the exponential factor e^{-ik} accounts for the fact that one of the two atoms is moved to the next unit cell. Here, we consider the case of spin-0 quasiparticles (Bloch electrons without spin-orbit coupling), hence $G(k)$ does not contain a spin part. Now, since $G^2(k) = \sigma_0 e^{-ik}$ the eigenvalues of G are $\pm e^{-ik/2}$, i.e., we can label the two bands of $H(k)$ by the eigenvalues of $G(k)$

$$G\,|\psi_\pm(\mathbf{k})\rangle = \pm e^{-ik/2}\,|\psi_\pm(\mathbf{k})\rangle\,, \tag{39}$$

cf. Eq. (37) with $n = 2$ and $p = 1$. We see that the eigenvalues are momentum dependent and change from $\pm$ at $k = 0$ to $\mp$ at $k = 2\pi$, as we go through the BZ. Hence, the two eigenspaces get interchanged and the bands must cross at least once, see Fig. 7.

It is also possible to mathematically prove that there needs to be at least one crossing [16]. The proof is by contradiction. First, we observe that $G(k)$ does not commute with σ_3 (it anti-commutes). Therefore, $\mathcal{H}(k)$ cannot contain a term proportional to σ_3, since it is symmetry forbidden. Moreover, we can drop terms proportional to the identity, since they only shift the energy of the eigenstates, but do not alter the band crossings. For this reason the Hamiltonian can be assumed to be off-diagonal and can be written as

$$H(k) = \begin{pmatrix} 0 & q(k) \\ q^*(k) & 0 \end{pmatrix}. \tag{40}$$

With this parametrization, the spectrum of $\mathcal{H}(k)$ is symmetric around $E = 0$ and is given by $E = \pm|q(k)|$. For this reason, any band crossing must occur at $E = 0$. Applying the symmetry constraint (38), we find that $q(k)$ must satisfy

$$q(k)e^{ik} = q^*(k). \tag{41}$$

We now need to show that any periodic function $q(k)$ satisfying the constraint (41) must have zeros, corresponding to a band crossing point. To see this, we introduce the complex variable

[8] Here we assume that here are no additional degeneracies due to other symmetries.

$z := e^{ik}$ and the complex function $f(z) := q(k)$. From Eq. (41) it follows that $zf(z) = f^*(z)$. Assuming that $f(z)$ is nonzero on the unit circle S^1, then

$$z = f^*(z)/f(z), \tag{42}$$

which, however, leads to a contradiction. This is because for $z \in S^1$ the two sides of Eq. (42) both define functions from S^1 to S^1. But the left hand side has winding number 1, while the right hand side has *even* winding number, since $f^*(z)/f(z) = e^{-2i\text{Arg}[f(z)]}$. Thus, $f(z)$ and $q(k)$ must vanish at some k by contradiction. Therefore, there must be a band crossing point somewhere in the BZ.

3.2 Weyl nodal-line semimetal

Next we discuss how a glide reflection symmetry can enforce two-fold degeneracies along a line. Materials with these line degeneracies are called Weyl nodal-line semimetals. For concreteness, we consider a system with spin-orbit coupling, which is invariant under the hexagonal SG 190 ($P\bar{6}2c$). This SG contains a glide reflection symmetry of the form

$$M_x \ : \ (x, y, z) \to (-x, y, z + \tfrac{1}{2})i\sigma_x, \tag{43}$$

where the Pauli matrix σ_x operates in spin space. Applying this glide reflection twice yields minus a unit translation in the x direction, i.e., $-\hat{T}_x$, where the minus sign is due to the spin part. The glide reflection (43) leaves two planes in the BZ invariant, namely the $k_x = 0$ plane and the $k_x = \pi$ plane, see Fig. 9(a).

3.2.1 Symmetry eigenvalues

We now use the arguments from Sec. 3.1 to show that the glide reflection M_x leads to symmetry-enforced degeneracies along a line within the $k_x = \pi$ plane. Within the $k_x = \pi$ plane, the Bloch bands can be chosen to be eigenstates of M_x with the eigenvalues

$$M_x \left|\psi_\pm(\mathbf{k})\right\rangle = \pm ie^{-ik_z/2} \left|\psi_\pm(\mathbf{k})\right\rangle, \tag{44}$$

which follows from Eq. (37) with $p = 1$ and $n = 2$. Next, we add time-reversal symmetry to the game, since we want to study nonmagnetic systems. Time-reversal symmetry sends the crystal momentum $\mathbf{k}$ to $-\mathbf{k}$ and acts on the Hamiltonian as (see Sec. 2.1.1)

$$\mathcal{T}^{-1} H(-\mathbf{k}) \mathcal{T} = +H(\mathbf{k}), \tag{45}$$

with the operator $\mathcal{T} = i\sigma_y \mathcal{K}$ and $\mathcal{K}$ the complex conjugation operator. Time-reversal symmetry leaves two points in the $k_x = \pi$ plane invariant [blue and red dots in Fig. 9(a)], which are called time-reversal invariant momenta (TRIMs). At these TRIMs the bands are two-fold degenerate due to Kramers theorem, i.e., they form Kramers pairs. Away from the TRIMs, however, the bands are in general non-degenerate. (Note that spin-orbit coupling lifts the spin degeneracy.) Since $\mathcal{T}$ contains the complex conjugation operator $\mathcal{K}$, the Kramers pairs at the TRIMs are

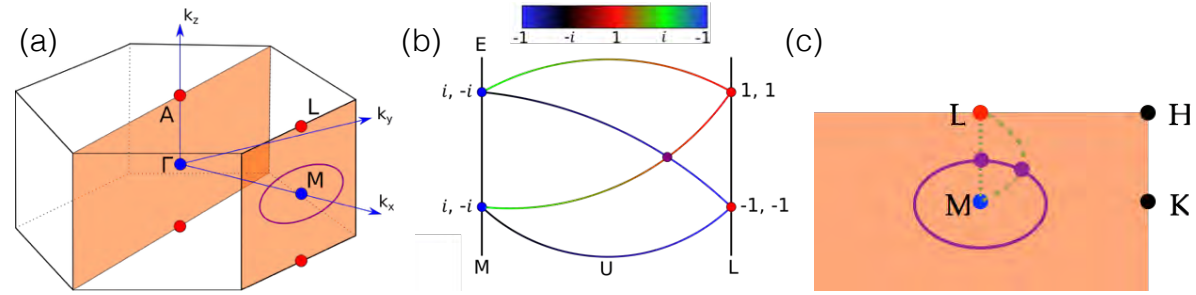

Fig. 9: *(a) Weyl nodal line in the $k_x = \pi$ plane protected by the glide mirror symmetry M_x, Eq.* (43)*. (b) Band connectivity diagram for a line connecting M and L within the $k_x = \pi$ plane, which is left invariant by M_x. The bands are Kramers degenerate at M and L. The color shading indicates the M_x eigenvalues* (44) *of the Bloch bands. (c) The Bloch bands along any path within the $k_x = \pi$ plane, connecting M to L, exhibit the band connectivity shown in (b). Figures adapted from Ref. [21].*

formed by bands whose M_x eigenvalues are complex conjugate pairs. Using Eq. (44), we find that at the L point of the $k_x = \pi$ plane the M_x eigenvalues are $+1$ and -1, while at the M point they are $+i$ and $-i$. (Similar arguments hold for the TRIMs in the $k_x = 0$ plane.) Hence, at M the Kramers pairs are formed by bands with opposite M_x eigenvalues [blue dot in Fig. 9(a)], while at L they are formed by bands with the same M_x eigenvalues [red dot in Fig. 9(a)]. This is shown in Fig. 9(b), where the M_x eigenvalues are indicated by the color shading. We see that since the Kramers pairs switch partners as we go from M to L, the bands must cross at least once forming a group of four connected bands with an *hourglass dispersion*. Because this holds for any one-dimensional path within the $k_x = \pi$ plane, connecting M to L, the $k_x = \pi$ plane must contain a Weyl line degeneracy, as shown in Fig. 9(c).

3.2.2 Compatibility relations

The existence of symmetry-enforced band crossings can also be inferred from the compatibility relations between irreducible representations (irreps) at different high-symmetry points of the BZ [37]. To show this we consider again a system in SG 190 with spin-orbit coupling. But before doing so, we first need to review some basic properties of double SGs and their double-valued irreps [38].

Band structures of nonmagnetic materials with spin-orbit coupling (i.e., materials with a time-reversal symmetry $\mathcal{T}^2 = -1$) are invariant under the symmetries of *double* SGs. Correspondingly, the symmetry operators under which these band structures transform are given by the *double-valued* irreps of the double SGs. If we consider the band structure at a particular high-symmetry point $\mathbf{k}$ (or high-symmetry line), then the symmetries are reduced to a subgroup of the double SG. This subgroup is denoted by $\mathcal{G}_\mathbf{k}$ and is called the little group at $\mathbf{k}$. Because the Bloch Hamiltonian restricted to $\mathbf{k}$ commutes with this little group $\mathcal{G}_\mathbf{k}$, the bands at $\mathbf{k}$ can be labeled by the double valued irreps of $\mathcal{G}_\mathbf{k}$, which are denoted by $\bar{\mathbf{D}}_\mathbf{k}$. If we move continuously away from a high-symmetry point $\mathbf{k}_1$ to a nearby point $\mathbf{k}_2$, then the symmetries are lowered. That is,

Irreps \Element	E	M_x
$\overline{M}_5$	$\begin{pmatrix}+1 & 0\\ 0 & +1\end{pmatrix}$	$\begin{pmatrix}+i & 0\\ 0 & -i\end{pmatrix}$
$\overline{L}_2$	$+1$	-1
$\overline{L}_3$	$+1$	-1
$\overline{L}_4$	$+1$	$+1$
$\overline{L}_5$	$+1$	$+1$
$\overline{C}'_3$	$+1$	$e^{\frac{i}{2}(\pi+k_z)}$
$\overline{C}'_4$	$+1$	$e^{-\frac{i}{2}(\pi-k_z)}$

Table 2: *Double valued irreps of SG 190 ($P\bar{6}2c$) without time-reversal at the TRIMs M and L and within the mirror plane $k_z = \pi$, denoted by C'. Due to the partial translation of M_x, the irreps for C' have momentum-dependent phases. For the labeling of the irreps we use the convention of Ref. [37].*

the little group $\mathcal{G}_{\mathbf{k}_2}$ is smaller than the little group $\mathcal{G}_{\mathbf{k}_1}$, and forms a subgroup $\mathcal{G}_{\mathbf{k}_2} \subset \mathcal{G}_{\mathbf{k}_1}$. As a consequence, representations $\widetilde{\mathbf{D}}_{\mathbf{k}_2}$ of $\mathcal{G}_{\mathbf{k}_2}$ can be inferred (i.e., subduced) from the little-group irreps $\bar{\mathbf{D}}_{\mathbf{k}_1}$, i.e., we have

$$\widetilde{\mathbf{D}}_{\mathbf{k}_2} = \bar{\mathbf{D}}_{\mathbf{k}_1} \downarrow \mathcal{G}_{\mathbf{k}_2}. \tag{46}$$

Decomposing the subduced representations $\widetilde{\mathbf{D}}_{\mathbf{k}_2}$ into irreps yields the compatibility relations between the irreps $\bar{\mathbf{D}}_{\mathbf{k}_1}$ and $\bar{\mathbf{D}}_{\mathbf{k}_2}$ [37–39]. From these compatibility relations one can deduce the connectivity of the Bloch bands in the BZ.

We will now show how this works for SG 190. We start be determining the little group irreps at the TRIMs M and L, and within the mirror plane $k_x = \pi$ (denoted by C'). Table 2 lists the double-valued irreps without time-reversal symmetry. We find that at the M point there is only one double-valued irrep, namely $\bar{M}_5$, which is two-dimensional and pseudoreal. At the L point there are four different irreps: $\bar{L}_2$, $\bar{L}_3$, $\bar{L}_4$, and $\bar{L}_5$, which are one-dimensional and complex. The irreps for C' are all one-dimensional and have $\mathbf{k}$-dependent phases, due to the translation part of the glide reflection M_x, Eq. (43). At the TRIMs M and L we need to construct time-reversal symmetric irreps (i.e., real irreps) using Table 2. We note that pseudoreal irreps are time-reversal symmetric by themselves. Complex irreps, on the other hand, must be paired up into complex-conjugate pairs to make them time-reversal symmetric [38, 39]. Hence, at the L point we need to pair $\bar{L}_2$ with $\bar{L}_3$ and $\bar{L}_4$ with $\bar{L}_5$, see Fig. 10(a). With this, all time-reversal symmetric irreps at the TRIMs are two dimensional, in agreement with the Kramers theorem, which leads to two-fold degeneracies. As we move away from the TRIMs to a point in C', these two-dimensional irreps decompose into one-dimensional irreps, in such a way that the compatibility relations are satisfied.

To figure out how the Kramers pairs split up, we therefore need to derive the compatibility relations between the irreps at M, L, and C'. For this purpose, we use the following relation

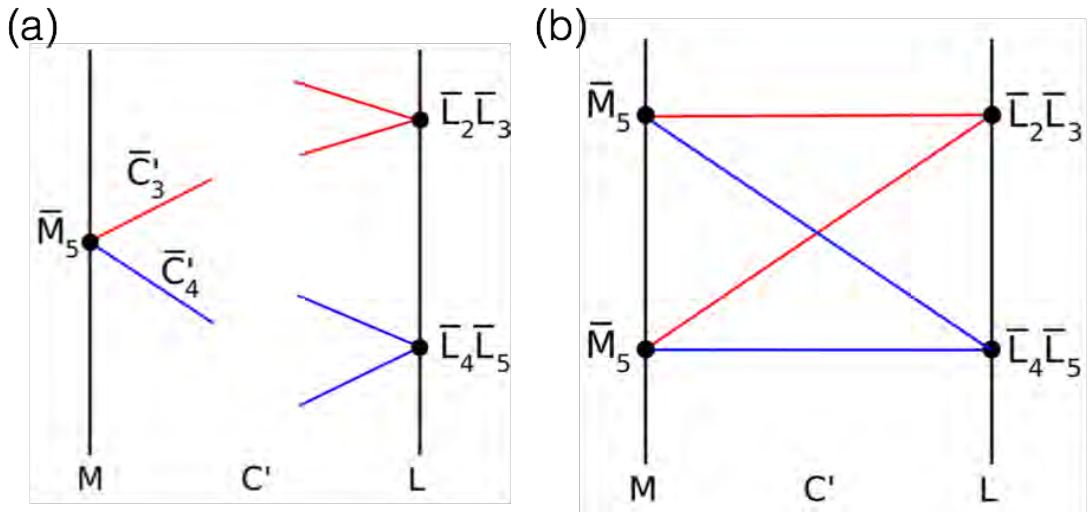

Fig. 10: *(a) Compatibility relations for SG 190 between the little-group irreps at M, L, and C' ($k_x = \pi$ plane). (b) Band connectivity diagram for SG 190 for a path within the $k_x = \pi$ plane connecting M to L. Figures adapted from Ref. [21].*

between the characters χ of the irreps[9]

$$\chi[\overline{D}_l(g)] = \sum_{i=1}^{2} \chi[\overline{C}'_{m_i}(g)], \tag{47}$$

for any group element g. Here, $\chi[\overline{D}_l(g)]$ is the character of the irrep $\overline{D}_l$ at the TRIM M or L, while $\{\overline{C}'_{m_1}, \overline{C}'_{m_2}\}$ is the set of irreps that $\overline{D}_l$ decomposes into, as we move away from the TRIMs to a point on C'. Relation (47) follows from continuity, which requires that the characters of the irreps are preserved, as we continuously move away from a TRIM to a point on C'. By use of Eq. (47), we infer that the time-reversal symmetric irrep at M (where $k_z = 0$) decomposes into

$$\overline{M}_5 \;\rightarrow\; \overline{C}'_3 + \overline{C}'_4, \tag{48a}$$

while for the real irreps at L (where $k_z = \pi$) we have

$$\begin{aligned} \overline{L}_2\overline{L}_3 &\;\rightarrow\; \overline{C}'_3 + \overline{C}'_3, \\ \overline{L}_4\overline{L}_5 &\;\rightarrow\; \overline{C}'_4 + \overline{C}'_4. \end{aligned} \tag{48b}$$

The above two relations represent the compatibility relations between the irreps at the TRIMs (M and L) and C'. They determine the connectivity of the bands on the path M–C'–L. That is, as we move from M to C' and then on to L, the Kramers pairs at M must split up and then pair up again, such that the compatibility relations (48) are satisfied. Therefore the bands must connect as shown in Fig. 10(b). That is, the irreps switch partners as we move within C' from M to L. As a consequence, the band connectivity is nontrivial with sets of four connected bands that show an hourglass dispersion, with at least one movable crossing between M and L. Hence, each quartet of bands within the C' plane forms at least one Weyl nodal line, which fully agrees with the results of Sec. 3.2.1, cf. Fig. 9(b).

[9]The character of a group irrep associates with each group element the trace of the corresponding irrep matrix.

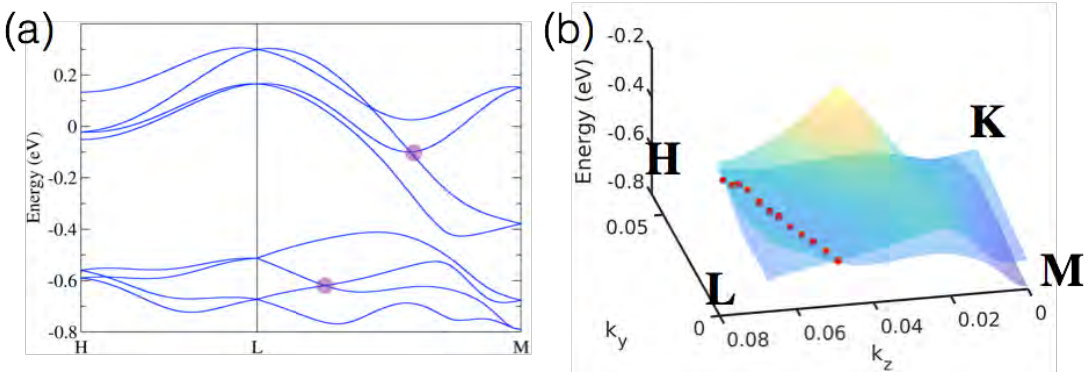

Fig. 11: *(a) Electronic band structure of ZrIrSn along the high-symmetry path H–L–M, cf. Fig 9. The band crossings along M–L (violet dots) are part of Weyl nodal lines within the $k_x = \pi$ plane. (b) Dispersion of the pair of bands that form the Weyl nodal line at $E \simeq -0.64$ eV. The nodal line (red dots) encloses the L point.*

3.2.3 Example material: ZrIrSn

Having found that all band structures with strong spin-orbit coupling in SG 190 exhibit Weyl nodal lines, we now apply the strategy of page 19 to find real materials that exhibit these line degeneracies. To do so, we consult the ICSD database (https://icsd.fiz-karlsruhe.de) to find materials with heavy elements (indicating strong spin-orbit coupling) that crystallize in SG 190. This was performed in Ref. [21] and it was found that ZrIrSn is a good example. ZrIrSn contains only heavy elements resulting in strong spin-orbit coupling. Indeed, the calculated band structure [Fig. 11(a)] shows that the spin-orbit coupling leads to a large band splitting away from the TRIMs, by about 100 meV. As predicted in the previous section, along the M–L path we observe groups of four connected bands with an hourglass dispersion and at least one crossing. As shown in Fig. 11(b), these crossings are part of Weyl nodal lines in the C' plane, i.e., two-fold degeneracies on rings which enclose one of the TRIMs.
Similar to the Dirac nodal-line semimetal of Sec. 2.3, the topology of this Weyl nodal ring is described by a π Berry phase [33], which leads to drumhead surface states. Furthermore, the bands that form nodal rings carry large Berry curvatures, which leads to anomalous transport properties, for example, anomalous magnetoelectric responses or large Hall effects.

3.3 Dirac nodal-line semimetal

As a second example, we study how off-center symmetries can enforce four-fold degeneracies along a line, i.e., how they can enforce the existence of Dirac nodal lines. In Sec. 2.3, we have already discussed a Dirac nodal-line semimetal with an *accidental* nodal ring, which is protected by symmorphic symmetries (i.e., reflection or $\mathcal{PT}$ symmetry). Here, however, we discuss Dirac nodal lines that are *symmetry enforced* by off-center symmetries. Moreover, we shall consider systems with strong spin-orbit coupling, which was neglected in Sec. 2.3. For concreteness, we consider spin-orbit coupled systems which are symmetric under the hexagonal SG 176 ($P6_3/m$). This SG contains the glide reflection

$$\widetilde{M}_z \;:\; (x, y, z) \to (x, y, -z + \tfrac{1}{2}) i\sigma_z, \tag{49a}$$

where σ_z acts in spin space, and the inversion symmetry

$$P \ : \ (x, y, z) \to (-x, -y, -z). \tag{49b}$$

These two symmetries form together a pair of so-called off-center symmetries [20, 21]. We observe hat the translation part $\mathbf{t} = \frac{1}{2}\hat{z}$ of the glide reflection (49a) is perpendicular to the $\widetilde{m}_z$ invariant space (i.e., the xy mirror plane). As mentioned on page 20, this type of glide reflection can be transformed into a symmorphic symmetry by a different choice of unit cell i.e., by shifting the origin by $\frac{1}{4}\hat{z}$. However, this shift in origin also affects P, leading to a translation part in P. Since $\widetilde{M}_z$ and P have different reference points, it is not possible to choose the origin such that both $\widetilde{M}_z$ and P are without translation parts. A pair of two such symmetries with different reference points are called *off-center symmetries*.

3.3.1 Commutation relations

We now show that the momentum dependence of the commutation relation between $\widetilde{M}_z$ and P enforces the existence of fourfold degenerate nodal-lines. The glide reflection $\widetilde{M}_z$ leaves two planes in the hexagonal BZ invariant, namely the $k_x = 0$ plane and the $k_x = \pi$ plane, see Fig. 12(a). Within these planes the Bloch states can be labeled by the $\widetilde{M}_z$ eigenvalues $\pm i$ (remember that $\widetilde{M}_z^2 = -1$). I.e., we have

$$\widetilde{M}_z \left|\psi_\pm(\mathbf{k})\right\rangle = \pm i \left|\psi_\pm(\mathbf{k})\right\rangle . \tag{50}$$

To derive the commutation relation between $\widetilde{M}_z$ and P, we apply the symmetry operators $\widetilde{M}_z$ and P in succession,

$$\begin{aligned}
&(x, y, z) \xrightarrow{P} (-x, -y, -z) \xrightarrow{\widetilde{M}_z} (-x, -y, +z + \tfrac{1}{2}) i\sigma_z, \\
&(x, y, z) \xrightarrow{\widetilde{M}_z} (x, y, -z + \tfrac{1}{2}) i\sigma_z \xrightarrow{P} (-x, -y, +z - \tfrac{1}{2}) i\sigma_z.
\end{aligned}$$

This tells us that $\widetilde{M}_z P$ and $P\widetilde{M}_z$ differ by a unit translation in the z direction. Hence, by letting $\widetilde{M}_z P$ and $P\widetilde{M}_z$ act on the Bloch states (50), we get the commutation relation in $\mathbf{k}$-space

$$\widetilde{M}_z P \left|\psi_\pm(\mathbf{k})\right\rangle = e^{ik_z} P \widetilde{M}_z \left|\psi_\pm(\mathbf{k})\right\rangle . \tag{51}$$

It follows that the two symmetry operators commute in the $k_z = 0$ plane, while they anticommute in the $k_z = \pi$ plane. Since we are interested in nonmagnetic systems, we now also need to study the commutation relation between the off-center symmetries (49) and the time-reversal operator $\mathcal{T} = i\sigma_y \mathcal{K}$. Because $\mathcal{T}$ commutes with both $\widetilde{M}_z$ and P, we have

$$\widetilde{M}_z P\mathcal{T} \left|\psi_\pm(\mathbf{k})\right\rangle = e^{ik_z} P\mathcal{T} \widetilde{M}_z \left|\psi_\pm(\mathbf{k})\right\rangle . \tag{52}$$

Thus, the Kramers pair $\left|\psi_\pm(\mathbf{k})\right\rangle$ and $P\mathcal{T}\left|\psi_\pm(\mathbf{k})\right\rangle$ have the same $\widetilde{M}_z$ eigenvalues for $k_z = \pi$ (since $\widetilde{M}_z \left[P\mathcal{T}\left|\psi_\pm(\mathbf{k})\right\rangle\right] = -P\mathcal{T}\left[\pm i\left|\psi_\pm(\mathbf{k})\right\rangle\right] = \pm iP\mathcal{T}\left|\psi_\pm(\mathbf{k})\right\rangle$), while for $k_z = 0$, they have opposite $\widetilde{M}_z$ eigenvalues. Hence, if two Kramers pairs of bands with opposite $\widetilde{M}_z$ eigenvalues

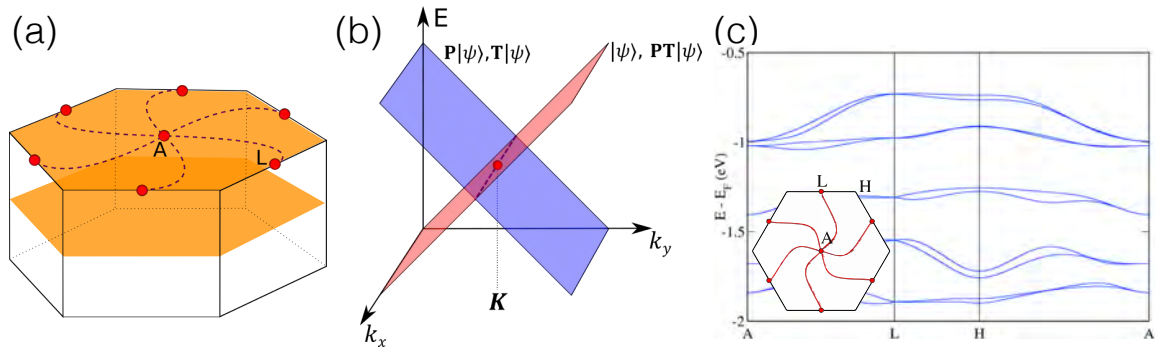

Fig. 12: *(a) Dirac nodal-lines in the $k_z = \pi$ plane, which connect the A and L points. (b) Two Kramers degenerate bands with opposite $\widetilde{M}_z$ eigenvalues cross each other to form a Dirac nodal line. (c) Electronic band structure of $LaBr_3$ along the high-symmetry path A–L–H–A. The band crossings along H–A are part of Dirac nodal lines within the $k_z = \pi$ plane. The inset shows the shape of the Dirac nodal line for the two top most bands in the main panel. Figures adapted from Ref. [21].*

cross within the $k_z = \pi$ plane, they form a Dirac nodal line. This Dirac nodal line cannot gap out, since the two Kramers pairs have opposite $\widetilde{M}_z$ eigenvalues. For $k_z = 0$, however, the crossing of two Kramers pairs of bands is not protected, since the two Kramers pairs have the same $\widetilde{M}_z$ eigenvalue.

Such a Dirac nodal line is in fact required to exist by symmetry alone, i.e., it occurs in any material with the off-center symmetries $(\widetilde{M}_z, P)$ and, in particular, in any material with spin-orbit coupling crystallizing in SG 176, irrespective of the chemical composition. To show that the Dirac nodal line is symmetry enforced, we consider the degeneracies at the TRIMs within the $k_z = \pi$ plane, i.e., at A and L [Fig. 12(a)]. At these two TRIMs the bands are four-fold degenerate, i.e., they form quartets of four degenerate states, which have the $\widetilde{M}_z$ eigenvalues

$$\widetilde{M}_z\,|\psi_\pm(\mathbf{K})\rangle = \pm i\,|\psi_\pm(\mathbf{K})\rangle\,, \tag{53a}$$
$$\widetilde{M}_z P\,|\psi_\pm(\mathbf{K})\rangle = \mp iP\,|\psi_\pm(\mathbf{K})\rangle\,, \tag{53b}$$
$$\widetilde{M}_z \mathcal{T}\,|\psi_\pm(\mathbf{K})\rangle = \mp i\mathcal{T}\,|\psi_\pm(\mathbf{K})\rangle\,, \tag{53c}$$
$$\widetilde{M}_z P\mathcal{T}\,|\psi_\pm(\mathbf{K})\rangle = \pm iP\mathcal{T}\,|\psi_\pm(\mathbf{K})\rangle\,, \tag{53d}$$

where $\mathbf{K} \in \{\mathrm{A}, \mathrm{L}\}$. These four Bloch states are mutually orthogonal to each other, because they are either Kramers partners or they have opposite $\widetilde{M}_z$ eigenvalues. Moving away from the TRIMs, the degenerate quartet splits, in general, into two Kramers pairs of bands. Due to inversion and time-reversal symmetry, the dispersion of the Kramers pairs of bands is symmetric with respect to the TRIMs. That is, the Kramers pairs of bands at $\mathbf{K}+\mathbf{k}$ and $\mathbf{K}-\mathbf{k}$ have the same energy, but opposite $\widetilde{M}_z$ eigenvalues, as shown in Fig. 12(b). It now follows from continuity, that each quartet of states at $\mathbf{K}$ cannot exist in isolation, but must be part of a Dirac nodal line connecting two TRIMs, see Fig. 12(a). This Dirac nodal line must be symmetric under inversion, time-reversal, and all other point-group symmetries of the SG, but is otherwise free to move within the $k_z = \pi$ plane. That is, the Dirac nodal line is movable, but not removable. For SG 176, which has a sixfold rotation symmetry, the Dirac nodal lines are shaped like stars, see Figs. 12(a) and 12(c).

3.3.2 Example material: $LaBr_3$

We have shown that all materials crystallizing in SG 176 have star-shaped nodal lines within the $k_z = \pi$ plane. In order to look for materials, we consult again the ICSD database and search for compounds with heavy elements crystallizing in SG 176. In Ref. [21] it was found that $LaBr_3$ is a good example. Figure 12(c) shows the first-principles band structure of $LaBr_3$ along the high-symmetry lines A–L–H–A . All bands are Kramers degenerate, due to the presence of $P\mathcal{T}$ symmetry. Along the H–A line we observe band crossings, which are part of Dirac nodal lines, whose shape resembles a star [inset of Fig. 12(c)].

4 Conclusions and future directions

In this chapter, we have reviewed accidental and symmetry-enforced band crossings. We have presented a classification of accidental band crossings in terms of symmetries and we have discussed how nonsymmorphic symmetries can lead to symmetry-enforced band crossings. We have presented a number of examples, ranging from Weyl semimetals with point nodes to Dirac semimetals with line nodes. From these discussions it is clear that symmetry together with topology fundamentally restricts the possible forms of band structures, i.e., in particular, their connectivity and their degeneracies. We have discussed this in terms of the momentum dependence of the symmetry eigenvalues, and in terms of compatibility relations between irreducible representations. An alternative approach is to study the properties of symmetric Wannier functions, which form space group representations. In this approach topological bands are identified as those, whose symmetric Wannier functions are not exponentially localized [40]. Combining this with symmetry based indicators, it is possible to perform high-throughput searches for topological materials [41–43].

While topological band structures of time-reversal invariant materials have been investigated extensively, topological band structures of magnetic systems still need to be understood better. Another avenue for future research is the study of how electron-electron correlations change the topology of materials. On the one hand, correlations can connect two topological band structures (or phases) that are distinct in the single-particle picture, on the other hand they can give rise to entirely new topological phenomena [2]. Finally, on the experimental front, there is a crucial need for better topological materials. In particular semimetals, where the Fermi energy is closer to the band crossing, and where there are no other bands close to the Fermi energy. The reader is invited to look for new topological semimetals by himself using the strategy detailed on page 19.

Acknowledgments. The material presented in this chapter is based upon works I did together with my students and collaborators, in particular, Ching-Kai Chiu, Yang-hao Chan, Yuxin Zhao, Jonathan Zhang, Wenbin Rui, Leslie Schoop, and Maia Vergniory. I thank them for sharing ideas and for their efforts. I also thank the organizers of the 10th Autumn School on Correlated Electrons for the invitation to contribute to this lecture series.

References

[1] M.Z. Hasan and C.L. Kane, Rev. Mod. Phys. **82**, 3045 (2010)

[2] C.-K. Chiu, J.C.Y. Teo, A.P. Schnyder, and S. Ryu, Rev. Mod. Phys. **88**, 035005 (2016)

[3] G.E. Volovik: *Topology of quantum vacuum*, *Lecture Notes in Physics*, Vol. 870 (Springer Berlin, 2013)

[4] G.E. Volovik, Lect. Notes Phys. **718**, 31 (2007)

[5] N.P. Armitage, E.J. Mele, and A. Vishwanath, Rev. Mod. Phys. **90**, 015001 (2018)

[6] A. Burkov, Annu. Rev. Condens. Matter Phys. **9**, 359 (2018)

[7] S.-Y. Yang, H. Yang, E. Derunova, S.S.P. Parkin, B. Yan, and M.N. Ali, Advances in Physics: X **3**, 1414631 (2018)

[8] C. Herring, Phys. Rev. **52**, 365 (1937)

[9] X. Huang, L. Zhao, Y. Long, P. Wang, D. Chen, Z. Yang, H. Liang, M. Xue, H. Weng, Z. Fang, X. Dai, and G. Chen, Phys. Rev. X **5**, 031023 (2015)

[10] P. Liu, J.R. Williams, and J.J. Cha, Nature Reviews Materials **4**, 479 (2019)

[11] A.A. Burkov, Nat. Mater. **15**, 1145 (2016)

[12] P. Li, W. Wu, Y. Wen, C. Zhang, J. Zhang, S. Zhang, Z. Yu, S.A. Yang, A. Manchon, and X.-x. Zhang, Nat. Commun. **9**, 3990 (2018)

[13] Q. Wang, C.-Z. Li, S. Ge, J.-G. Li, W. Lu, J. Lai, X. Liu, J. Ma, D.-P. Yu, Z.-M. Liao, and D. Sun, Nano Letters **17**, 834 (2017)

[14] R. Lundgren, P. Laurell, and G.A. Fiete, Phys. Rev. B **90**, 165115 (2014)

[15] A. Yamakage, Y. Yamakawa, Y. Tanaka, and Y. Okamoto, J. Phys. Soc. Jpn. **85**, 013708 (2016)

[16] Y.X. Zhao and A.P. Schnyder, Phys. Rev. B **94**, 195109 (2016)

[17] L. Michel and J. Zak, Phys. Rev. B **59**, 5998 (1999)

[18] S.M. Young and C.L. Kane, Phys. Rev. Lett. **115**, 126803 (2015)

[19] A. Furusaki, Science Bulletin **62**, 788 (2017)

[20] B.-J. Yang, T.A. Bojesen, T. Morimoto, and A. Furusaki, Phys. Rev. B **95**, 075135 (2017)

[21] J. Zhang, Y.-H. Chan, C.-K. Chiu, M.G. Vergniory, L.M. Schoop, and A.P. Schnyder, Phys. Rev. Materials **2**, 074201 (2018)

[22] Y.-H. Chan, B. Kilic, M.M. Hirschmann, C.-K. Chiu, L.M. Schoop, D.G. Joshi, and A.P. Schnyder, Phys. Rev. Materials **3**, 124204 (2019)

[23] J. Singleton: *Band Theory and Electronic Properties of Solids* Oxford Master Series in Condensed Matter Physics (Oxford University Press, 2001)

[24] T. Ozawa, H.M. Price, A. Amo, N. Goldman, M. Hafezi, L. Lu, M.C. Rechtsman, D. Schuster, J. Simon, O. Zilberberg, and I. Carusotto, Rev. Mod. Phys. **91**, 015006 (2019)

[25] K. Li, C. Li, J. Hu, Y. Li, and C. Fang, Phys. Rev. Lett. **119**, 247202 (2017)

[26] H. Nielsen and M. Ninomiya, Nuclear Physics B **185**, 20 (1981)

[27] C.-K. Chiu and A.P. Schnyder, Phys. Rev. B **90**, 205136 (2014)

[28] T. Morimoto and A. Furusaki, Phys. Rev. B **88**, 125129 (2013)

[29] A.P. Schnyder, S. Ryu, A. Furusaki, and A.W.W. Ludwig, Phys. Rev. B **78**, 195125 (2008)

[30] S. Ryu, A.P. Schnyder, A. Furusaki, and A.W.W. Ludwig, New J. Phys. **12**, 065010 (2010)

[31] A. Altland and M.R. Zirnbauer, Phys. Rev. B **55**, 1142 (1997)

[32] M. Nakahara: *Geometry, Topology and Physics* (Tailor & Francis, New York, 2003)

[33] Y.-H. Chan, C.-K. Chiu, M.Y. Chou, and A.P. Schnyder, Phys. Rev. B **93**, 205132 (2016)

[34] D. Vanderbilt and R.D. King-Smith, Phys. Rev. B **48**, 4442 (1993)

[35] W.B. Rui, Y.X. Zhao, and A.P. Schnyder, Phys. Rev. B **97**, 161113 (2018)

[36] T. Matsushita, S. Fujimoto, and A.P. Schnyder, arXiv:2002.11666 (2020)

[37] L. Elcoro, B. Bradlyn, Z. Wang, M.G. Vergniory, J. Cano, C. Felser, B.A. Bernevig, D. Orobengoa, G. de la Flor, and M.I. Aroyo, J. Appl. Crystallogr. **50**, 1457 (2017)

[38] C. Bradley and A.P. Cracknell: *The Mathematical Theory of Symmetry in Solids: Representation theory for point groups and space groups* (Clarendon Press, Oxford, 1972)

[39] S.C. Miller and W.F. Love: *Tables of Irreducible Representations of Space Groups and Co-representations of Magnetic Groups* (Pruett, Boulder, 1967)

[40] J. Cano and B. Bradlyn, arXiv e-prints arXiv:2006.04890 (2020)

[41] M.G. Vergniory, L. Elcoro, C. Felser, N. Regnault, B.A. Bernevig, and Z. Wang, Nature **566**, 480 (2019)

[42] T. Zhang, Y. Jiang, Z. Song, H. Huang, Y. He, Z. Fang, H. Weng, and C. Fang, Nature **566**, 475 (2019)

[43] F. Tang, H.C. Po, A. Vishwanath, and X. Wan, Nat. Phys. **15**, 470 (2019)